Journal of Computational Physics **154,** 393–427 (1999)
Article ID jcph.1999.6320, available online at http://www.idealibrary.com on IDEAL®

The Ghost Fluid Method for Deflagration and Detonation Discontinuities

Ronald P. Fedkiw,*[,1] Tariq Aslam,†[,2] and Shaojie Xu‡[,3]

Department of Mathematics, University of California, Los Angeles, California 90095-1555; †Los Alamos National Laboratory, Los Alamos, New Mexico 87545; and ‡University of Illinois at Urbana–Champaign, Urbana, Illinois 61807

Received November 2, 1998; revised June 7, 1999

The level set method for multiphase compressible flows is simple to implement, especially in the presence of topological changes. However, this method was shown to suffer from large spurious oscillations. A new Ghost Fluid Method (GFM) was developed to remove these spurious oscillations by minimizing the numerical smearing in the entropy field with the help of an Isobaric Fix technique. The GFM was designed for traditional contact discontinuities where the interface moves with the fluid velocity only. In this paper, the GFM is extended to treat multimaterial interfaces where the interface velocity includes a regression rate due to the presence of chemical reactions converting one material into another. Specifically, interface models for deflagration and detonation discontinuities are considered. The resulting numerical method is robust and easy to implement.

1. INTRODUCTION

In [19], the authors applied the level set method to the multiphase compressible flow. The level set function was used as an indicator function and each grid point was designated as one fluid or the other in order to choose the appropriate equation of state. Then the numerical fluxes were formed and differenced in the usual manner; see, e.g., [24]. In [14], it was shown that this technique produced large spurious oscillations in the pressure and velocity fields. This problem was rectified in [12, 6, 5] with schemes that involved *explicit* treatment of the appropriate boundary conditions at the interface. As a consequence, these schemes are intricate in one dimension and can only be extended

[1] Research supported in part by the ONR under Grants N00014-97-1-0027 and N00014-97-1-0968.

[2] Research performed under the auspices of the U.S. Department of Energy.

[3] Research funded by the U.S. Department of Energy through the University of California under Subcontract B341494.

0021-9991/99 $30.00

to multiple dimensions with ill-advised dimensional splitting in time. In addition, multilevel time integrators, such as Runge–Kutta methods, are difficult to implement for these schemes.

The Ghost Fluid Method GFM [7] avoids the oscillations at multimaterial interfaces without *explicitly* applying the interface boundary conditions. Instead, the (GFM) creates an artificial fluid which *implicitly* captures the boundary conditions at the interface. In the flavor of the level set method which *implicitly* captures the location of the interface, the GFM *implicitly* captures the boundary conditions at the interface. Since the boundary conditions are *implicitly* captured by the construction of a ghost fluid, the overall scheme becomes easy to implement in multidimensions without time splitting. In addition, Runge–Kutta methods are trivial to apply.

In [7], the GFM was implemented for contact discontinuities where the interface moves at the fluid velocity only. In this case, the pressure and normal velocity of the ghost fluid are copied over from the real fluid in a node by node fashion while the entropy and tangential velocities are defined with the use of a simple partial differential equation for one-sided constant extrapolation in the normal direction. See [7] for details.

In this paper, the GFM is extended to multimaterial interfaces where the interface velocity includes a regression rate due to the presence of chemical reactions converting one material into another. Specifically, interface models for deflagration and detonation discontinuities are considered similar to the work in [25, 18, 26, 27], where the authors extended the level set method from [28] to interfaces that represent burning front discontinuities. In [28], the authors keep a sharp interface location using the level set function, while smearing out the surrounding flow variables, e.g., density. This numerical treatment is not acceptable for deflagration wave discontinuities since their propagation speed is evaluated as a function of the exact unburnt gas conditions which are lost when the state variables are smeared out. In [25, 18, 26, 27] the authors developed a new "in-cell reconstruction" technique that gives a sharp representation of the states on each side of the interface as needed for deflagration discontinuities. Those authors used the level set method to *implicitly* capture the interface location, while using the "in-cell reconstruction" technique to *explicitly* enforce the boundary conditions at the interface. The resulting algorithm is more efficient than standard interface tracking techniques, since the interface location is captured and not tracked. While the algorithm described in [25, 18, 26, 27] utilizes dimensional splitting in time, this is not a necessary condition for the "in-cell reconstruction" technique [15]. However, the boundary conditions are still *explicitly* applied. In contrast, the GFM *implicitly* captures the boundary conditions at the interface by the construction of a ghost fluid. The resulting numerical method is easy to implement in multidimensions (without time splitting) and extends trivially to Runge–Kutta methods.

2. EQUATIONS

2.1. *Euler Equations*

The basic equations for compressible flow are the Euler equations,

$$\mathbf{U}_t + \mathbf{F}(\mathbf{U})_x + \mathbf{G}(\mathbf{U})_y + \mathbf{H}(\mathbf{U})_z = 0, \tag{1}$$

which can be written in detail as

$$\begin{pmatrix} \rho \\ \rho u \\ \rho v \\ \rho w \\ E \end{pmatrix}_t + \begin{pmatrix} \rho u \\ \rho u^2 + p \\ \rho uv \\ \rho uw \\ (E+p)u \end{pmatrix}_x + \begin{pmatrix} \rho v \\ \rho uv \\ \rho v^2 + p \\ \rho vw \\ (E+p)v \end{pmatrix}_y + \begin{pmatrix} \rho w \\ \rho uw \\ \rho vw \\ \rho w^2 + p \\ (E+p)w \end{pmatrix}_z = 0, \tag{2}$$

where t is the time, (x, y, z) are the spatial coordinates, ρ is the density, $\mathbf{V} = \langle u, v, w \rangle$ are the velocities, E is the total energy per unit volume, and p is the pressure. The total energy is the sum of the internal energy and the kinetic energy is

$$E = \rho e + \frac{\rho(u^2 + v^2 + w^2)}{2}, \tag{3}$$

where e is the internal energy per unit mass. The two-dimensional Euler equations are obtained by setting $w = 0$, while the one-dimensional Euler equations are obtained by setting both $v = 0$ and $w = 0$.

The pressure can be written as a function of density and internal energy, $p = p(\rho, e)$. The speed of sound is defined by

$$c = \sqrt{p_\rho + \frac{p p_e}{\rho^2}}, \tag{4}$$

where p_ρ and p_e are partial derivatives of the pressure with respect to the density and internal energy, respectively.

For an ideal gas $p = \rho RT$, where $R = R_u / M$ is the specific gas constant with $R_u \approx 8.31451$ J/mol K the universal gas constant and M the molecular weight of the gas. Also valid for an ideal gas is $c_p - c_v = R$, where c_p is the specific heat at constant pressure and c_v is the specific heat at constant volume. Gamma is the ratio of specific heats, $\gamma = c_p / c_v$. For an ideal gas, one can write

$$de = c_v \, dT \tag{5}$$

and assuming that c_v does not depend on temperature (calorically perfect gas), integration yields

$$e = e_o + c_v T, \tag{6}$$

where e_o is not uniquely determined, and one could choose any value for e at 0 K (although one needs to use caution when dealing with more than one material to be sure that integration constants are consistent with the heat release in any chemical reactions that occur) [3].

Note that

$$p = \rho RT = \frac{R}{c_v} \rho(e - e_o) = (\gamma - 1)\rho(e - e_o) \tag{7}$$

is used later in the text.

2.2. *Level Set Equation*

We use the level set equation

$$\phi_t + \mathbf{W} \cdot \nabla \phi = 0 \tag{8}$$

to keep track of the interface location as the zero level of ϕ. In this equation, $\mathbf{W}$ is the level set velocity of the interface. In general ϕ starts out as the signed distance function, is advected by solving Eq. (8) using the methods in [11], and then is reinitialized using

$$\phi_t + S(\phi_o)(|\nabla \phi| - 1) = 0 \tag{9}$$

to keep ϕ approximately equal to the distance function (i.e., $|\nabla \phi| = 1$) near the interface where we need additional information. We note that our method allows us to solve Eq. (8) independently of the Euler equations. That is, Eq. (8) can be solved directly using the method in [11], and the eigensystem for the Euler equations does not depend on ϕ, since we will be solving only one phase problem with any given eigensystem (see the later sections). For more details on the level set function see [7, 19, 28].

3. THE GFM FOR A CONTACT DISCONTINUITY

The level set function is used to keep track of the interface. The zero level marks the location of the interface, while the positive values correspond to one fluid and the negative values correspond to the other fluid. Each fluid satisfies the Euler equations as described in the last section with different equations of state for each fluid. Based on the work in [11], the discretization of the level set function can be done independently of the two sets of Euler equations. Besides discretizing Eq. (8) one needs to discretize two sets of Euler equations. This is done with the help of ghost cells.

Any level set function defines two separate domains for the two separate fluids; i.e., each point corresponds to one fluid or the other. Ghost cells are defined at every point in the computational domain so that each grid point contains the mass, momentum, and energy for the real fluid that exists at that point (according to the sign of the level set function) and a ghost mass, momentum, and energy for the other fluid that does not really exist at that grid point (the fluid from the other side of the interface). Once the ghost cells are defined, one can use standard one-phase methods (e.g., see [24]) to update the Euler equations at every grid point for both fluids. Then the level set function is advanced to the next time step, and the sign of the level set function is used to determine which of the two sets of updated fluid values should be used as the real fluid values at each grid point.

Consider a general time integrator for the Euler equations. In general, one constructs right hand sides of the ordinary differential equations for both fluids based on the methods in [24]; then the level set function is advanced to the next time level and the sign of the level set function determines which of the two right hand sides to use in the time update for the Euler equations. This can be done for every step and every combination of steps in a multistep method.

Last, we note that only a band of three to five ghost cells on each side of the interface is actually needed by the computational method depending on the stencil and movement of the interface. One can optimize the code accordingly.

3.1. *Defining Values at the Ghost Cells*

In [7], the GFM was implemented for a contact discontinuity in the Euler equations. It was apparent that the pressure and normal velocity were continuous, while the tangential velocity was continuous in the case of a no-slip boundary condition at the interface but discontinuous for a shear wave. It was also apparent that the entropy was discontinuous.

For variables that are continuous across the interface, the ghost fluid values are set to be equal to the real fluid values at each grid point. Since these variables are continuous, this node by node population will implicitly capture the correct interface values of the continuous variables. This is the key mechanism in coupling the two distinct sets of Euler equations.

Note that the discontinuous variables are governed by a linearly degenerate eigenvalue. Thus, they move with the speed of the interface and information in these variables should not cross the interface. Moreover, these discontinuous variables should not be erroneously coupled or forced to be continuous across the interface, as is usually the case for many conventional numerical methods which produce spurious numerical dissipation at discontinuities, e.g., shock capturing methods. In order to avoid the numerical smearing of these variables, one-sided constant extrapolation is used to populate the values in the ghost fluid. Note that the work in [8] on the Isobaric Fix shows that one does not have to deal directly with the entropy. There are a few options for the choice of the variable used in extrapolation ranging from density to temperature.

The extrapolation of the discontinuous variables is carried out in the following fashion. Using the level set function, the unit normal is defined at every grid point as

$$\mathbf{N} = \frac{\nabla\phi}{|\nabla\phi|} = \langle n_1, n_2, n_3\rangle, \tag{10}$$

where $\mathbf{N}$ always points from the fluid with $\phi < 0$ into the fluid with $\phi > 0$. Then the advection equation

$$I_\tau \pm \mathbf{N}\cdot\nabla I = 0 \tag{11}$$

is solved in fictitious time τ for each variable I that needs to be extrapolated across the interface in one direction or the other. The "+" sign is used to populate the ghost fluid in the region where $\phi > 0$ with the values of I from the region where $\phi < 0$, while the real fluid values of I are kept fixed in the region where $\phi < 0$. Likewise, the "−" sign is used to populate the ghost fluid in the region where $\phi < 0$ with the values of I from the region where $\phi > 0$, while the real fluid values of I are kept fixed in the region where $\phi > 0$. This equation only needs to be solved for a few steps in fictitious time in order to populate a thin band of approximately three to five ghost cells needed for the numerical method.

Note that the above procedure does not apply an isobaric fix to the cells in the real fluid which borders the interface. In order to apply the isobaric fix, keep the real fluid values of I fixed in the region where $\phi < -\epsilon$ when using the "+" sign in Eq. (11), and keep the real fluid values of I fixed in the region where $\phi > \epsilon$ when using the "−" sign in Eq. (11). Since ϕ is an approximate distance function, choose ϵ to be the thickness of the band in which the isobaric fix is to be applied. We use $\epsilon = 1.5\Delta x$.

When the need arises to extrapolate the tangential velocity, first extrapolate the entire velocity fied, $\mathbf{V} = \langle u, v, w\rangle$. Then, at every cell in the ghost region there are two separate

velocity fields, one from the real fluid and one from the extrapolated fluid. For each velocity field, the normal component of velocity, $V_N = \mathbf{V} \cdot \mathbf{N}$, is put into a three component vector, $V_N\,\mathbf{N}$, and then a basis free projection method (see, e.g., [9]) is used to define the two dimensional velocity field in the tangent plane by another three component vector, $\mathbf{V} - V_N\,\mathbf{N}$. Finally, the normal component of velocity, $V_N\,\mathbf{N}$, from the real fluid is added to the tangential component of velocity, $\mathbf{V} - V_N\,\mathbf{N}$, from the extrapolated fluid to obtain the ghost fluid velocity that occupies the ghost cell.

Once the ghost fluid values are defined as outlined above, they can be use to assemble the conserved variables for the ghost fluid.

4. EXTENDING THE GHOST FLUID METHOD

For a simple contact discontinuity that moves with the speed of the fluid only, we were able to separate the variables into two sets based on their continuity at the interface. The continuous variables were copied into the ghost fluid in a node by node fashion in order to capture the correct interface values. The discontinuous variables were extrapolated in a one-sided fashion to avoid errors due to numerical dissipation. In order to apply this idea to a general interface moving at speed D in the normal direction, one needs to determine the continuous variables for this general interface problem.

Conservation of mass, momentum, and energy can be applied to an interface in order to abstract continuous variables. One can place a flux on the interface oriented tangent to the interface so that material that passes through this flux passes through the interface. This flux moves with speed D (the interface speed) in the normal direction, and the mass, momentum, and energy which flow into this flux from one side of the interface must flow back out the other side of the interface. That is, the mass, momentum, and energy flux in this moving reference frame are continuous variables. Otherwise, there would be a mass, momentum, or energy sink at the interface and conservation would be violated. We denote the mass, momentum, and energy flux in this moving reference frame as F_ρ, $\mathbf{F}_{\rho\mathbf{V}}$, and F_E, respectively. The statement that these variables are continuous is essentially equivalent to the Rankine–Hugoniot jump conditions at an interface moving with speed D in the normal direction. In [25, 18, 26, 27] the Rankine–Hugoniot jump conditions were explicitly applied to the interface. Instead, the Ghost Fluid Method uses the fact that F_ρ, $\mathbf{F}_{\rho\mathbf{V}}$, and F_E are continuous to define a ghost fluid that captures the interface values of these variables. That is, the Rankine–Hugoniot jump conditions are implicitly captured, resulting in a method that is robust and easy to implement.

Remark. Numerically F_ρ, $\mathbf{F}_{\rho\mathbf{V}}$, and F_E may not be continuous. This could occur from initial data or wave interactions. However, since F_ρ, $\mathbf{F}_{\rho\mathbf{V}}$, and F_E are treated as though they were continuous in the numerical method, numerical dissipation smooths them out. In fact, this numerical dissipation helps to guarantee the correct numerical solution.

Remark. The level set function is designed to represent interfaces where the interface crosses material at most once due to an entropy condition [21, 23]. Simple contact discontinuities that move with the local material velocity never cross over material. If one material is being converted into another, then the interface may include a regression rate for this conversion. If the regression rate for this conversion of one material into another is based on some sort of chemical reaction, then the interface can pass over a material exactly once, changing it into another material. The same chemical reaction cannot occur to a material

more than once, and the reverse reaction is usually not physical due to an entropy condition. However, in the case of reversible chemical reactions, the level set may pass over a material in one direction (the reaction) and then pass back over the same material in the opposite direction (the reverse reaction).

Remark. Shocks may be interpreted as the conversion of an uncompressed material into a compressed material. In this case, D is the shock speed and the GFM could be used to follow a lead shock, but since shocks can pass over a material more than once in the same direction, all subsequent shocks must be captured or modeled by separate level set functions. A simple example of the GFM for non-reactive shock waves is presented in a later section, although this approach will be examined in detail in a future paper [2].

Remark. In the general case, $\mathbf{F}_{\rho\mathbf{V}}$ and F_E will include general mechanical stress terms on the interface, e.g., viscosity, surface tension, and material models. In addition, F_E will include general thermal stress terms on the interface, e.g., thermal conductivity. General mechanical and thermal stress terms are not considered in this paper although pressure is considered as a mechanical stress.

To define F_ρ, $\mathbf{F}_{\rho\mathbf{V}}$, and F_E, we write the equations in conservation form for mass, momentum, and energy. The fluxes for these variables are then rewritten in the reference frame of a flux which is tangent to the interface by simply taking the dot product with the normal direction,

$$\langle \mathbf{F}(\mathbf{U}), \mathbf{G}(\mathbf{U}), \mathbf{H}(\mathbf{U}) \rangle \cdot \mathbf{N} = \begin{pmatrix} \rho \\ \rho \mathbf{V}^T \\ E + p \end{pmatrix} V_N + \begin{pmatrix} 0 \\ p\mathbf{N}^T \\ 0 \end{pmatrix}, \tag{12}$$

where $V_N = \mathbf{V} \cdot \mathbf{N}$ is the local fluid velocity normal to the interface and the superscript T designates the transpose. Then the measurements are taken in the moving reference frame (speed D) to get

$$\begin{pmatrix} \rho \\ \rho(\mathbf{V}^T - D\mathbf{N}^T) \\ \rho e + \frac{\rho|\mathbf{V} - D\mathbf{N}|^2}{2} + p \end{pmatrix} (V_N - D) + \begin{pmatrix} 0 \\ p\mathbf{N}^T \\ 0 \end{pmatrix}, \tag{13}$$

from which we define

$$F_\rho = \rho(V_N - D) \tag{14}$$

$$\mathbf{F}_{\rho\mathbf{V}} = \rho(\mathbf{V}^T - D\mathbf{N}^T)(V_N - D) + p\mathbf{N}^T \tag{15}$$

$$F_E = \left(\rho e + \frac{\rho|\mathbf{V} - D\mathbf{N}|^2}{2} + p \right)(V_N - D) \tag{16}$$

as continuous variables for use in the GFM. That is, we will define the ghost fluid in a node by node fashion by solving the system of equations

$$F_\rho^G = F_\rho^R \tag{17}$$

$$\mathbf{F}_{\rho\mathbf{V}}^G = \mathbf{F}_{\rho\mathbf{V}}^R \tag{18}$$

$$F_E^G = F_E^R \tag{19}$$

at each grid point. Note that the superscript R stands for a real fluid value at a grid point, while the superscript G stands for a ghost fluid value at a grid point. Since F_ρ^R, $\mathbf{F}_{\rho\mathbf{v}}^R$, F_E^R, $\mathbf{N}$, and D are known at each grid point, these can be substituted into Eqs. (17), (18), and (19), leaving ρ^G, $\mathbf{V}^G$, p^G, and e^G undetermined. Since the ghost fluid is supposed to represent the real fluid on the other side of the interface, we use that fluid's equation of state as our sixth equation. Thus, populating the ghost nodes requires the solution of six algebraic equations with six unknowns at each grid point in a band about the interface. For many applications, this is rather trivial compared to applying the Rankine–Hugoniot jump conditions explicitly to the interface.

5. DEFINING THE INTERFACE SPEED D

The interface speed is usually a function of the surrounding materials. For example, in the case of a simple contact discontinuity, D can be defined as the continuous normal velocity of the two materials at the interface.

In order to update Eq. (8) for the level set function, one needs to define the level set velocity, $\mathbf{W}$, at every grid point. In the level set capturing framework, $\mathbf{W}$ is defined everywhere by a function which is continuous in the normal direction and has an interface value that moves the interface at the correct interface velocity. This global definition of $\mathbf{W}$ can be used to find D for use in solving Eqs. (17), (18), and (19). In a node by node fashion, $D = \mathbf{W} \cdot \mathbf{N}$ is defined as the velocity of the interface in the normal direction, capturing the correct value of D at the interface.

In many cases, D is given and one can define $\mathbf{W} = D\mathbf{N}$. Note that starting with $\mathbf{W}$, defining $D = \mathbf{W} \cdot \mathbf{N}$, and then defining $\mathbf{W} = D\mathbf{N}$ result in $\mathbf{W} = \mathbf{W}\,\mathbf{N}^T\mathbf{N}$, where the superscript T represents the transpose. While this equation is obviously false, both $\mathbf{W}$ and $\mathbf{W}\,\mathbf{N}^T\mathbf{N}$ behave the same with regard to the level set method. That is,

$$\phi_t + \mathbf{W} \cdot \nabla\phi = 0 \tag{20}$$

and

$$\phi_t + (\mathbf{W}\,\mathbf{N}^T\mathbf{N}) \cdot \nabla\phi = 0 \tag{21}$$

will be analytically equivalent, although there may be numerical differences.

5.1. *A Simple Contact Discontinuity*

Consider the case of a simple contact discontinuity where the interface moves with the local fluid velocity, i.e., $\mathbf{W} = \mathbf{V}$. Then $D = V_N^R$ is the component of the real fluid velocity normal to the interface at each point. Equation (17) becomes

$$\rho^G \left(V_N^G - V_N^R\right) = 0, \tag{22}$$

implying that $V_N^G = V_N^R$. That is, the normal component of the ghost fluid velocity should be equal to the normal component of the real fluid velocity at each point. Then Eq. (18) becomes $p^G = p^R$, implying that the pressure of the ghost fluid should be equal to the pressure of the real fluid at each point. Equation (19) is then trivially satisfied, leaving a degree of freedom. As discussed in [7], the entropy should be extrapolated in the normal direction along with an Isobaric Fix [8] to minimize "overheating." In addition, the tangential velocities are

extrapolated for a shear wave or copied over in a node by node fashion to enforce continuity of the tangential velocities for a "no-slip" boundary condition.

5.2. *Defining the Level Set Velocity* **W**

One issue that needs to be addressed in the level set formulation is the definition of the level set velocity $\mathbf{W}$ for use in Eq. (8). In the case of a simple contact discontinuity, $\mathbf{W} = \mathbf{V}$ is just the local fluid velocity. In more general cases, the interface speed may be a function of the variables on both sides of the interface and a general method for constructing $\mathbf{W}$ is needed.

Consider an interface separating two materials with states represented by $\mathbf{U}^{(1)}$ on one side of the interface and $\mathbf{U}^{(2)}$ on the other side of the interface. In general, the velocity of the interface can be defined by $\mathbf{W} = \mathbf{W}(\mathbf{U}^{(1)}_{int}, \mathbf{U}^{(2)}_{int})$ where the "*int*" subscript represents a variable that has been interpolated to the interface in a one-sided fashion. Generally, $\mathbf{W}$ is a continuous function and application of $\mathbf{W} = \mathbf{W}(\mathbf{U}^{(1)}, \mathbf{U}^{(2)})$ in a node by node fashion will capture the correct value of $\mathbf{W}$ at the interface.

In order to apply $\mathbf{W} = \mathbf{W}(\mathbf{U}^{(1)}, \mathbf{U}^{(2)})$ in a node by node fashion, one needs values of $\mathbf{U}^{(1)}$ and $\mathbf{U}^{(2)}$ at every node. $\mathbf{U}^{(1)}$ can be extended across the interface into the region occupied by $\mathbf{U}^{(2)}$, and $\mathbf{U}^{(2)}$ can be extended across the interface into the region occupied by $\mathbf{U}^{(1)}$. Then, every grid point in a band about the interface has values of both $\mathbf{U}^{(1)}$ and $\mathbf{U}^{(2)}$ to use when defining $\mathbf{W} = \mathbf{W}(\mathbf{U}^{(1)}, \mathbf{U}^{(2)})$. For first order accuracy, one can take a few time steps in fictitious time τ for the advection equation,

$$I_\tau \pm \mathbf{N} \cdot \nabla I = 0, \tag{23}$$

for each variable I that needs to be extrapolated. The "$\pm$" sign is chosen in the appropriate way to extend the components of $\mathbf{U}^{(1)}$ or of $\mathbf{U}^{(2)}$.

In general, one only needs extension for a thin band consisting of about three to five grid cells near the interface. Once the velocity is computed near the interface, it can be extended to cover the entire domain using Eq. (23) with I equal to each component of $\mathbf{W}$ and the appropriate choices of the "$\pm$" sign. Instead of extending $\mathbf{W}$ throughout the domain, one could use fast local level set methods in a narrow band about the interface; see, e.g., [1] and the references therein.

In some cases, D is preferable to $\mathbf{W}$ and one can use $\mathbf{D} = \mathbf{D}(\mathbf{U}^{(1)}_{int}, \mathbf{U}^{(2)}_{int})$ in a node by node fashion and then construct $\mathbf{W} = D\mathbf{N}$.

6. A NOTE ON CONSERVATION

The GFM decomposes the computational domain into separate regions for each fluid and utilizes a standard conservative flux differencing scheme for each separate fluid. This procedure creates nonunique fluxes at the interfaces separating different fluids and leads to a formal lack of discrete conservation on a set of measure zero near the interface. In addition, there is a lack of conservation due to the advection of the level set function similar to that in the area loss problem seen in incompressible flow calculations [28]. In [7], these conservation errors were discussed and numerical examples were provided to illustrate convergence to the correct weak solution for a variety of examples. Since the level set function is advected with the desired velocity of the discontinuity, one can still use this method to treat general discontinuities such as shocks. That is, the interface profile is not

smeared out and one does not have to rely on exact conservation to obtain the correct propagation speed for the discontinuity. This methodology is common in front tracking schemes; for example, [22] uses a nonconservative method for updating the location of the discontinuity and then formally corrects the conservation errors with a post-processing procedure [4]. It seems likely that a similar post-processing procedure could be developed to make the GFM fully conservative as well.

7. EXAMPLES

Consider an interface separating two materials with states represented by $\mathbf{U}^{(1)}$ on one side of the interface and $\mathbf{U}^{(2)}$ on the other side of the interface. Equation (23) is used to extend $\mathbf{U}^{(1)}$ and $\mathbf{U}^{(2)}$ so that both functions are defined on a five grid cell band near the interface. Then $D = (\mathbf{U}^{(1)}, \mathbf{U}^{(2)})$ is applied in a node by node fashion throughout the five grid cell band and $\mathbf{W} = D\mathbf{N}$ is defined within the band. The components of $\mathbf{W}$ can be extended throughout the domain using Eq. (23). However, in the sense of a local level set method, one does not need to extend $\mathbf{W}$ and we set $\mathbf{W} = 0$ outside our narrow band as opposed to extending it.

We experienced a small increase in computational overhead associated with the numerical treatment of the scalar level set equation and the equations for reinitialization and ghost cell population. Theoretically, these algorithms can be performed on a lower dimensional subset of the mesh; see, for example, [1] and the references therein. While our codes did not use narrow band methods for the standard level set equations, we did apply all ghost cell related algorithms in a thin band about the interface, increasing the computational cost by only a few percentage points over a standard one phase calculation in most cases.

Note that all our numerical examples use third order TVD Runge–Kutta and third order ENO–LLF [24].

7.1. *Non-reacting Shocks*

Consider the representation of a lead shock by a level set function where the positive values of ϕ correspond to the unshocked material and the negative values of ϕ correspond to the shocked material. Then the normal, $\mathbf{N}$, points from the shocked material into the unshocked material.

In one spatial dimension, the normal velocity is defined as $V_N = \mathbf{V} \cdot \mathbf{N}$ and Eqs. (14), (15), and (16) become

$$F_\rho = \rho(V_N - D) \tag{24}$$

$$\mathbf{F}_{\rho\mathbf{V}} = \rho(u - D\mathbf{N}^T)(V_N - D) + p\mathbf{N}^T \tag{25}$$

$$F_E = \left(\rho e + \frac{\rho|u - D\mathbf{N}|^2}{2} + p\right)(V_N - D), \tag{26}$$

where it is useful to define

$$F_{\rho\mathbf{V}_N} = \mathbf{N}\mathbf{F}_{\rho\mathbf{V}} = \rho(V_N - D)^2 + p \tag{27}$$

and to rewrite Eq. (26) as

$$F_E = \left(\rho e + \frac{\rho(V_N - D)^2}{2} + p\right)(V_N - D), \tag{28}$$

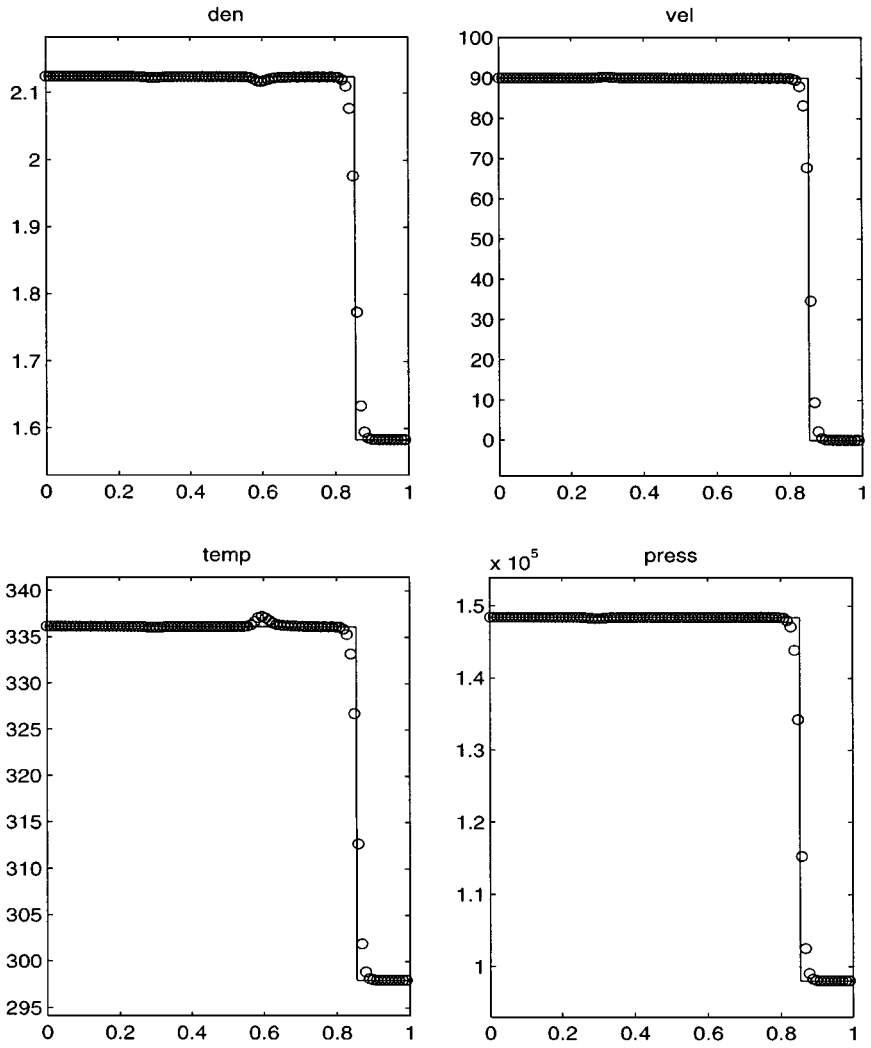

FIG. 1. Single shock (shock capturing scheme—ENO).

using the fact that $\mathbf{N} = \pm 1$ in one dimesnion. Then Eqs. (17), (18), and (19) can be written as

$$\rho^G \left(V_N^G - D\right) = F_\rho^R \tag{29}$$

$$\rho^G \left(V_N^G - D\right)^2 + p^G = F_{\rho \mathbf{V}_N}^R \tag{30}$$

$$\left(\rho^G e^G + \frac{\rho^G \left(V_N^G - D\right)^2}{2} + p^G\right)\left(V_N^G - D\right) = F_E^R, \tag{31}$$

where F_ρ^R, $F_{\rho \mathbf{V}_N}^R$, F_E^R, and D can be evaluated at each grid point. Adding the equation of state for the ghost fluid as

$$p^G = (\gamma^G - 1)\rho^G e^G \tag{32}$$

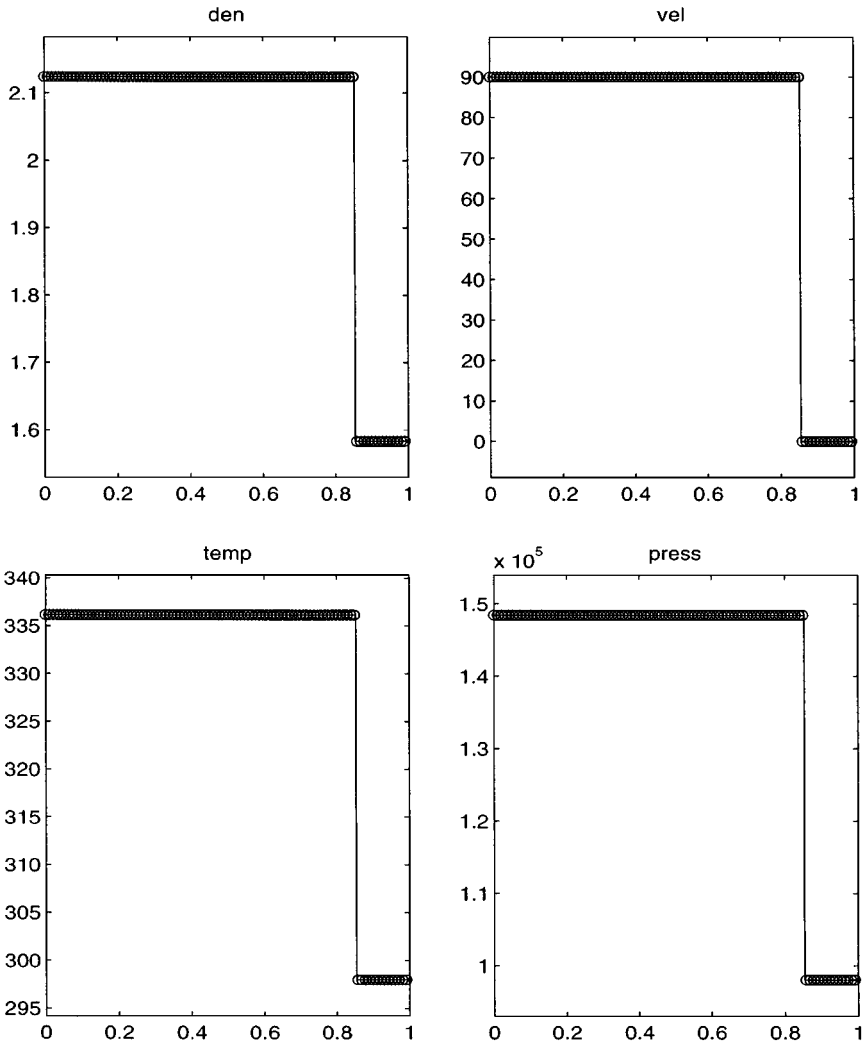

FIG. 2. Single shock (ghost fluid method).

yields four equations for four unknowns which can be arranged into a quadratic for $V_N^G - D$, where

$$V_N^G - D = \frac{\gamma^G F^R_{\rho \mathbf{V}_N}}{(\gamma^G + 1)F^R_\rho} \pm \sqrt{\left(\frac{\gamma^G F^R_{\rho \mathbf{V}_N}}{(\gamma^G + 1)F^R_\rho}\right)^2 - \frac{2(\gamma^G - 1)F^R_E}{(\gamma^G + 1)F^R_\rho}} \tag{33}$$

expresses the two solutions. Choosing one of these two solutions for V_N^G allows one to obtain ρ^G from Eq. (29), p^G from Eq. (30), and e^G from Eq. (32). In addition, $u^G = V_N^G \mathbf{N}$.

In order to choose the correct solution from Eq. (33), one has to know whether or not the ghost fluid is an unshocked fluid or a shocked fluid. Node by node, the real values of the unshocked fluid are used to create a shocked ghost fluid to help in the discretization of the shocked real fluid. Likewise, the real values of the shocked fluid are used to create an unshocked ghost fluid to help in the discretization of the unshocked real fluid.

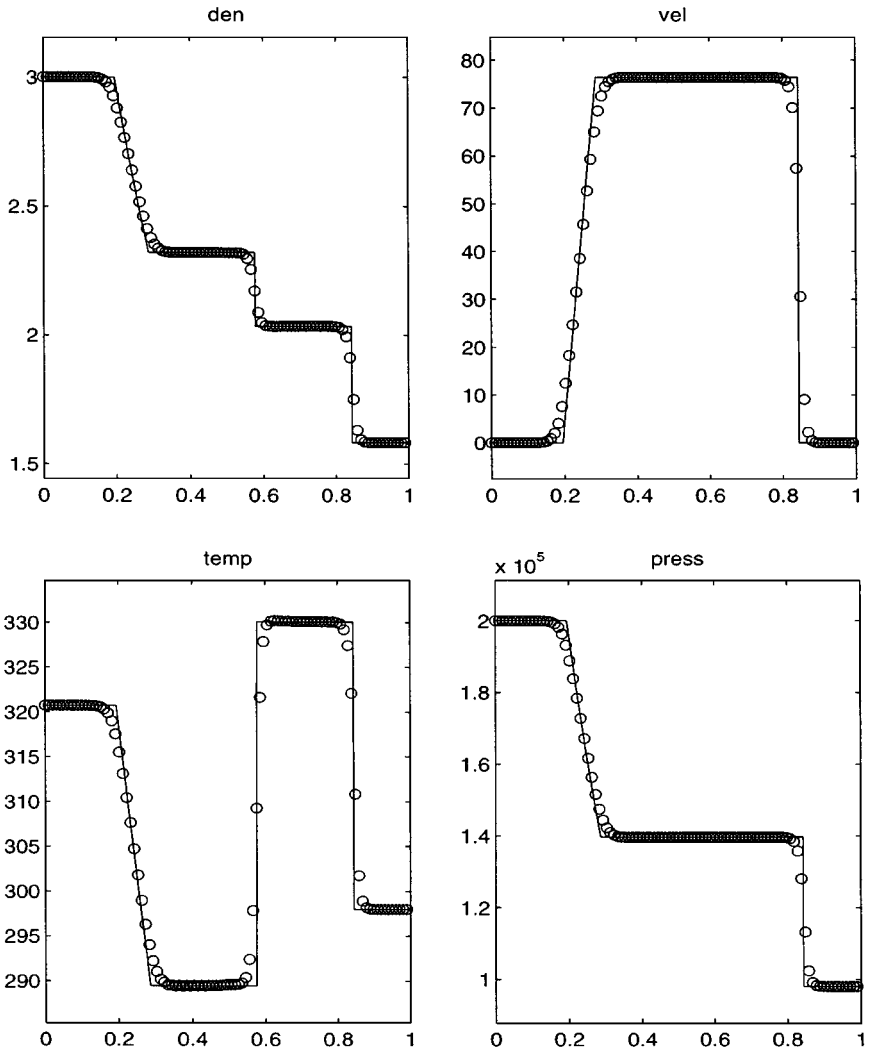

FIG. 3. Shock tube (shock capturing scheme—ENO)—100 grid points.

If the ghost fluid is a shocked fluid, then D should be subsonic relative to the flow, i.e., $V_N^G - c^G < D < V_N^G + c^G$ or $|V_N^G - D| < c^G$. On the other hand, if the ghost fluid is an unshocked fluid, then D should be supersonic relative to the flow, i.e., $|V_N^G - D| > c^G$. Therefore, one should choose the "$\pm$" sign in Eq. (33) to give the minimum value of $|V_N^G - D|$ when constructing a shocked ghost fluid and the maximum value of $|V_N^G - D|$ when constructing an unshocked ghost fluid.

For a simple non-reacting shock, the shock speed D can be defined directly from the mass balance equation as

$$D = \frac{\rho^{(1)}u^{(1)} - \rho^{(2)}u^{(2)}}{\rho^{(1)} - \rho^{(2)}} \tag{34}$$

in a node by node fashion. However, this simple definition of the shock speed will

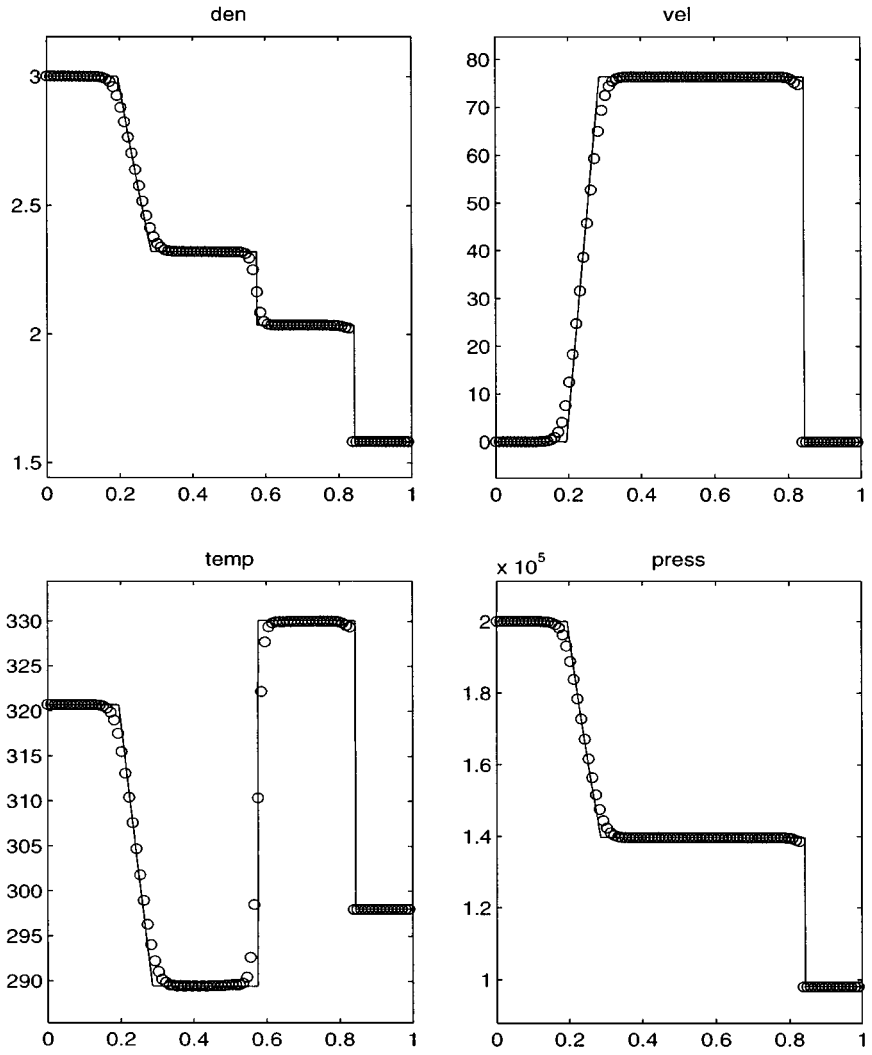

FIG. 4. Shock tube (ghost fluid method)—100 grid points.

erroneously give $D = 0$ in the case of a standard shock tube problem where both fluids are initially at rest. A somewhat better estimate of the shock speed can be derived by combining Eq. (34) with the momentum balance equation to get

$$D = \sqrt{\frac{\rho^{(1)}\left(u^{(1)}\right)^2 + p^{(1)} - \rho^{(2)}\left(u^{(2)}\right)^2 - p^{(2)}}{\rho^{(1)} - \rho^{(2)}}}, \tag{35}$$

where the shock speed is now dependent on the pressure as well. Note that Eqs. (34) and (35) are approximations for D. Clearly, these approximations will lead to nonphysical values of D in certain situations. In fact, D could be infinite or imaginary. A more robust, but still approximate, value for D can be obtained by evaluating $D = V_N + c$ with the Roe average of $\mathbf{U}^{(1)}$ and $\mathbf{U}^{(2)}$, since this is the exact shock speed for an isolated shock wave and never becomes ill-defined. Of course, the best definition of the shock speed can be derived by solving the Riemann problem for the states $\mathbf{U}^{(1)}$ and $\mathbf{U}^{(2)}$, although this

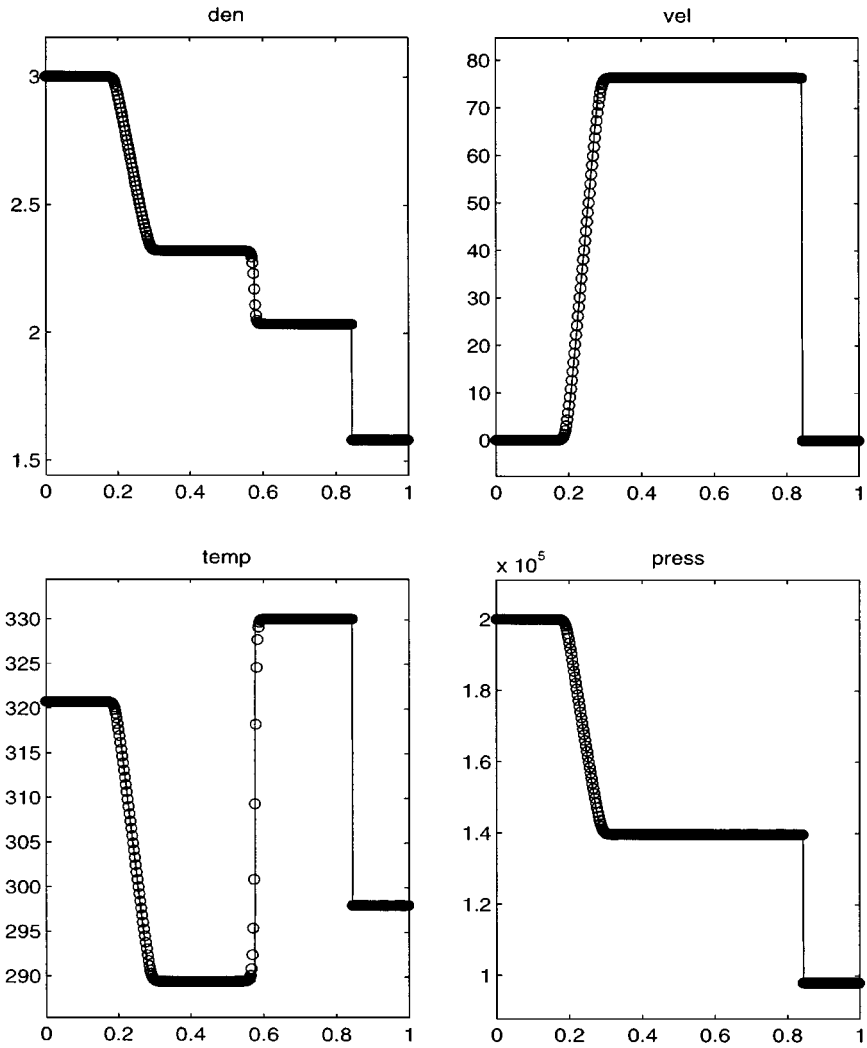

FIG. 5. Shock tube (ghost fluid method)—400 grid points.

generally requires an iteration procedure. In fact, this approach will be followed in a future paper [2].

7.1.1. EXAMPLE 1. In this example, we consider a single shock wave moving to the right, taken from [27]. We use a 1 m domain with 100 grid points and the interface located at $x = 0.5$ m, which is exactly midway between the 50th and 51st grid points. We use $\gamma = 1.4$ and $M = 0.040$ kg/mol for both gases. Initially, we set $\rho = 2.124$ kg/m^3, $u = 89.981$ m/s, and $p = 148{,}407.3$ Pa on the left, and $\rho = 1.58317$ kg/m^3, $u = 0$ m/s, and $p = 98{,}066.5$ Pa on the right.

Figure 1 shows the solution at $t = 0.001$ s with a standard shock capturing scheme, specifically third order ENO–LLF. Since the shock capturing scheme employs numerical differencing across the discontinuous shock wave, a large amount of numerical dissipation smears out the discontinuous shock structure. The shock capturing method does not identify the discontinuous initial data as a shock wave, but instead interprets it as a Riemann problem

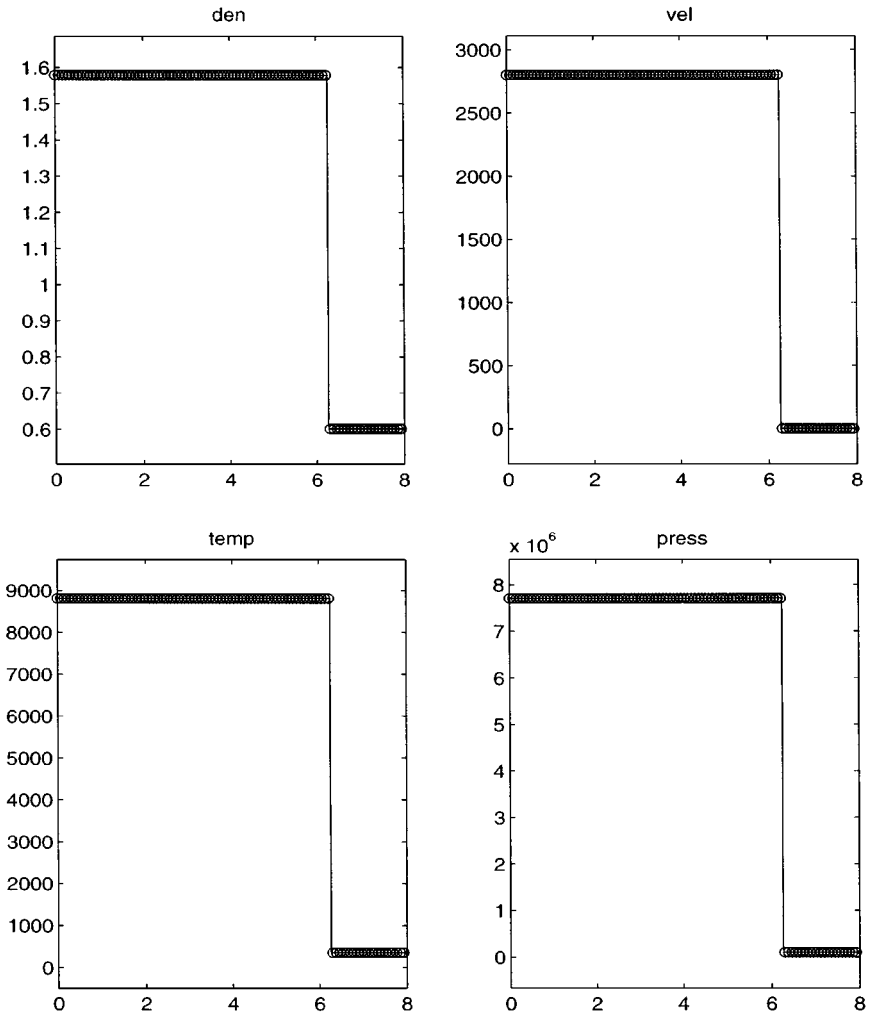

FIG. 6. Overdriven detonation.

and attempts to break it up into distinct waves one of which is a smeared out shock wave. The other waves are represented by the glitch near $x = 0.6$ in the density and temperature contained in the linearly degenerate field and the small glitch near $x = 0.3$ in all variables contained in the other truly nonlinear fields. These glitches are traditionally referred to as start-up errors and tend to diminish in size as the grid is refined.

Figure 2 shows the numerical solution computed with Eq. (35) as the shock speed for the GFM. Note that the GFM avoids numerical dissipation at the interface and the related artifacts, i.e., start-up errors. The GFM can interpret the discontinuous initial data as a shock wave and does not need to modify the shock profile in order to capture it.

The exact solution is plotted as a solid line in both figures.

7.1.2. EXAMPLE 2. Next, we set up a shock tube problem by changing the left state in Example 1 to $\rho = 3$ kg/m^3, $u = 0$ m/s, and $p = 2 \times 10^5$ Pa while still plotting the results at $t = 0.001$ s. The results with a standard shock capturing scheme are shown in Fig. 3 and those with the GFM and Eq. (35) are shown in Fig. 4. Note that the shock wave in the GFM case trails by one grid point and that there is a small glitch on the left hand side of

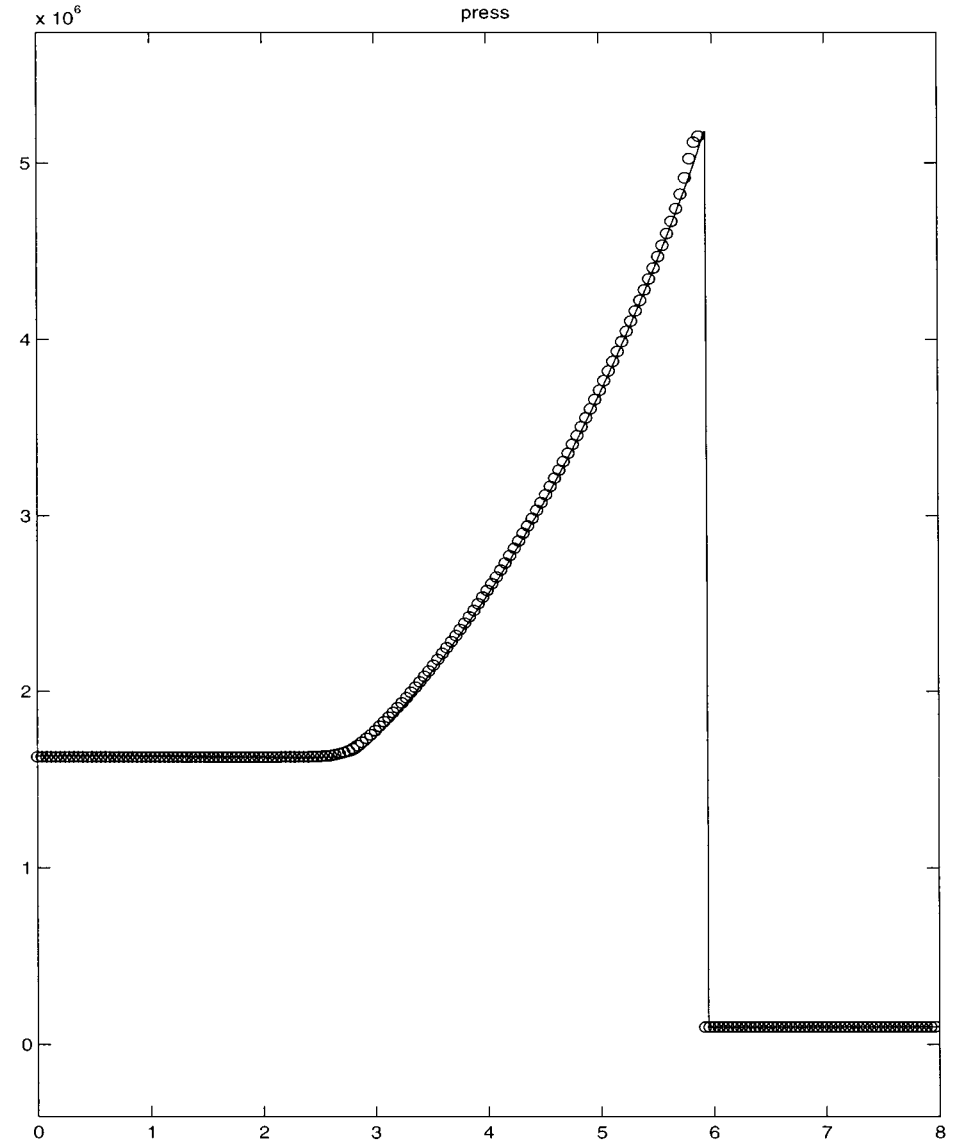

FIG. 7. Overdriven detonation at $t = 0.00135$ s.

the shock that disappears when the shock equilibrates later in time. These are first order numerical errors along the lines of the first order numerical smearing present in a shock capturing method. A more resolved calculation will achieve a flat profile in a shorter time; e.g., the same calculation with 400 grid points has the shock wave in the correct cell and no visible glitch, as can be seen in Fig. 5. The exact solution is plotted as a solid line in all three figures. For more details on the convergence and the location of discontinuities using the GFM, see [7].

7.2. *Detonations*

Strong detonations and Chapman–Jouguet detonations can be approximated as reacting shocks under the assumption that the reaction zone has negligible thickness. Let the

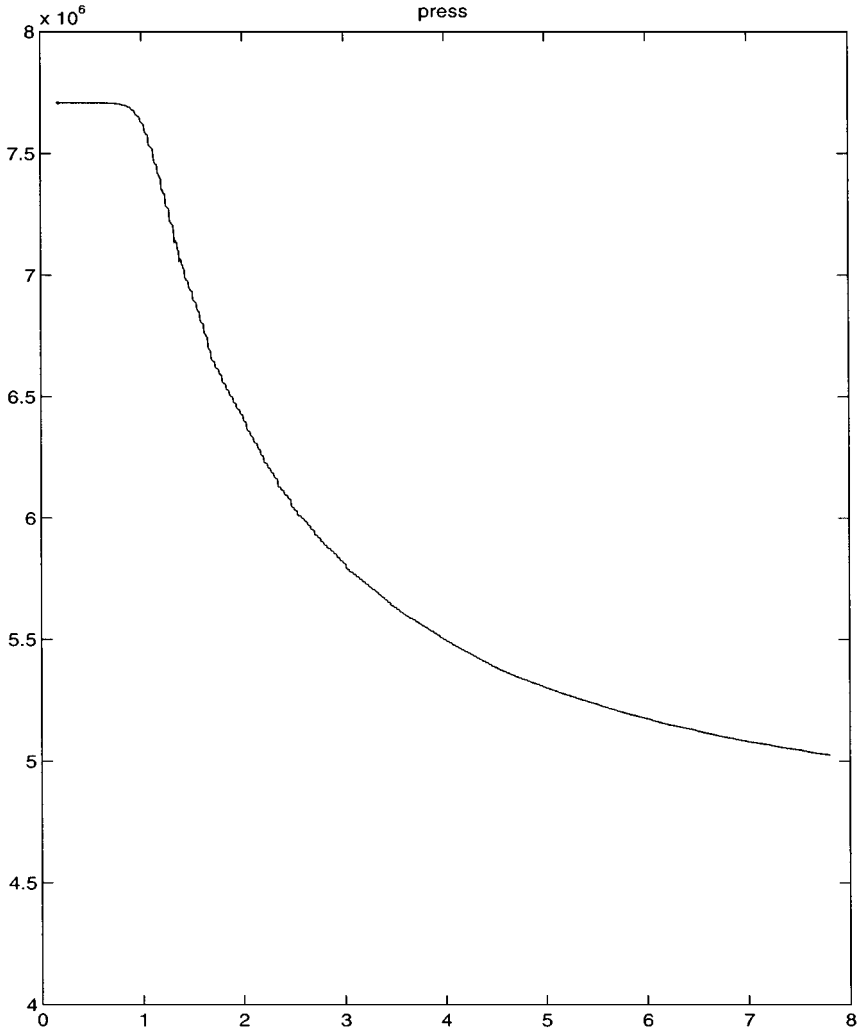

FIG. 8. Spatial history of the peak pressure.

unreacted material be represented by the positive values of ϕ and the reacted material be represented by the negative values of ϕ so that the normal, **N**, points from the reacted material into the unreacted material.

Equations (29), (30), and (31) are still valid, while Eq. (32) becomes

$$p^G = (\gamma^G - 1)\rho^G\left(e^G - e_o^G\right), \tag{36}$$

where one can no longer set $e_o = 0$ for both fluids. In detonations, the jump in e_o across the reaction front indicates the energy release in the chemical reaction. Equation (33) becomes

$$V_N^G - D = \frac{\gamma^G F_{\rho \mathbf{V}_N}^R}{(\gamma^G + 1)F_\rho^R} \pm \sqrt{\left(\frac{\gamma^G F_{\rho \mathbf{V}_N}^R}{(\gamma^G + 1)F_\rho^R}\right)^2 - \frac{2(\gamma^G - 1)}{(\gamma^G + 1)}\left(\frac{F_E^R}{F_\rho^R} - e_o^G\right)}, \tag{37}$$

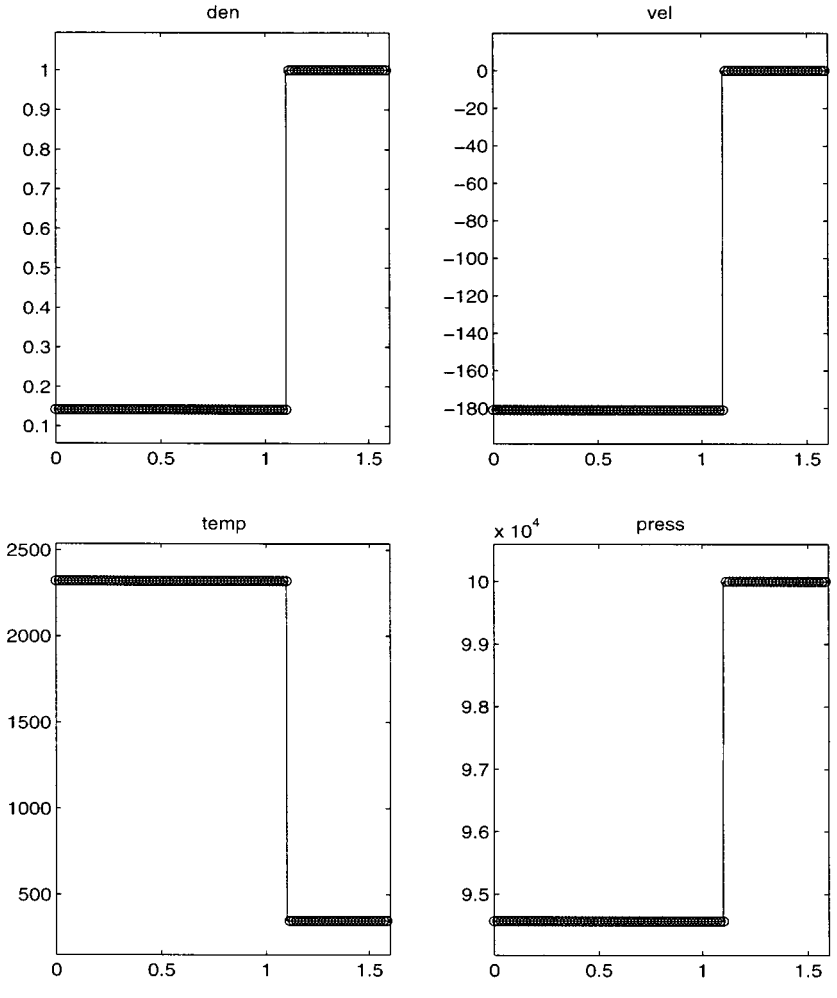

FIG. 9. Deflagration wave.

where one chooses the "±" sign to give the minimum value of $|V_N^G - D|$ when constructing a reacted ghost fluid and the maximum value of $|V_N^G - D|$ when constructing an unreacted ghost fluid. Equation (35) is used for the detonation speed D, although one may wish to consult a Riemann solver; e.g., see [29].

7.2.1. EXAMPLE 3. In this example, a single overdriven detonation wave moving to the right is taken from [18]. We use an 8 m domain with 100 grid points and the interface located at $x = 4$ m, which is exactly midway between the 50th and 51st grid points. We use $\gamma = 1.27$ in both gases, while $M = 0.015$ kg/mol in the unburnt gas and $M = 0.018$ kg/mol in the burnt gas. Initially, we set $\rho = 1.57861$ kg/m^3, $u = 2799.82$ m/s, and $p = 7{,}707{,}520$ Pa on the left, and $\rho = 0.601$ kg/m^3, $u = 0$ m/s, and $p = 1 \times 10^5$ Pa on the right. In addition, we have $e_o = \frac{242{,}000}{0.018}$ J/kg in the unburnt gas and $e_o = 0$ in the burnt gas. Figure 6 shows the solution at $t = 0.0005$ s after it has moved from $x = 4$ m to about $x = 6.26$ m at a speed of about 4521 m/s. The exact solution is plotted as a solid line in the figure.

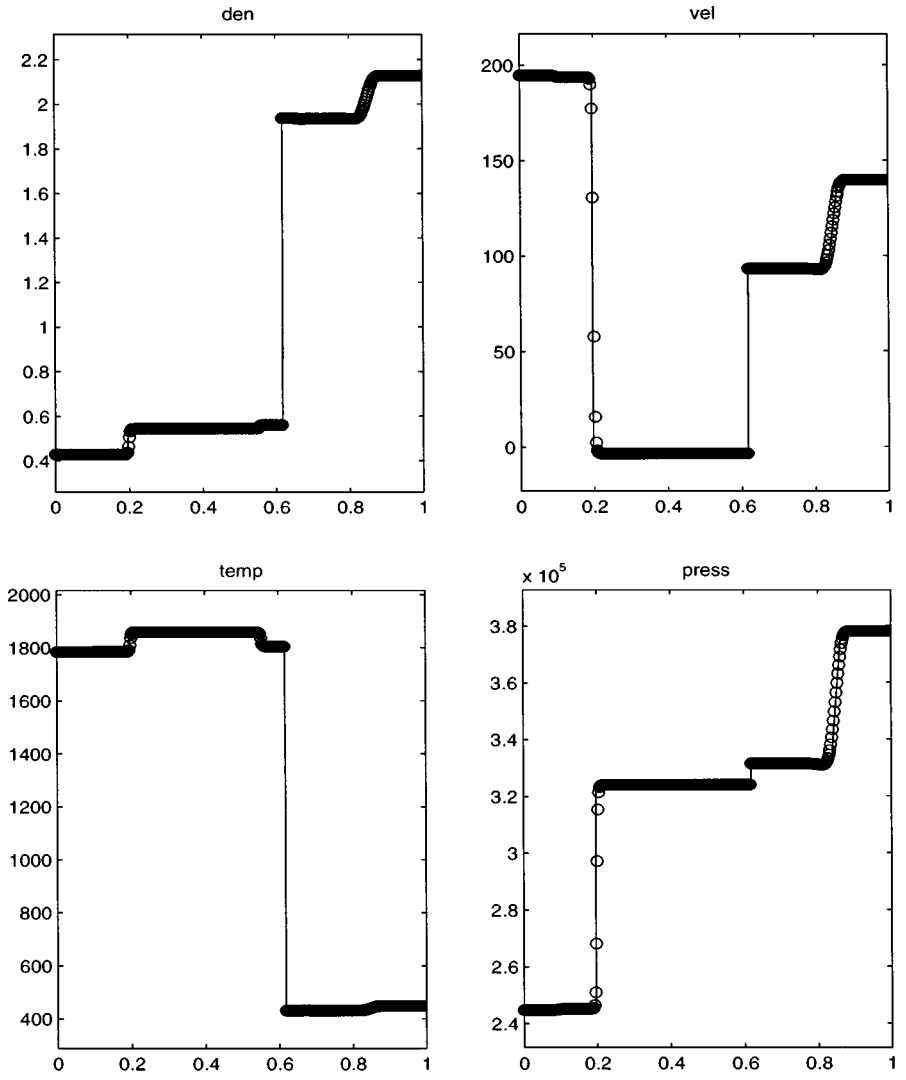

FIG. 10. Deflagration interaction with a leftgoing shock.

7.2.2. EXAMPLE 4. Next, we take the overdriven detonation from Example 3 with 200 grid cells (201 grid points) and start the detonation at $x = 0.175$ m, which is between the 5th and 6th grid points. A solid wall boundary condition is enforced at $x = 0$, creating a rarefaction wave that will catch up with the overdriven detonation and weaken it to a Chapman–Jouguet detonation as in [18]. The large circles in Fig. 7 show the pressure profile at $t = 0.00135$ s. The solid line in Fig. 7 shows the same calculation with an increased resolution of 800 grid cells (801 grid points), in which case the detonation wave starts exactly between the 18th and 19th grid points. Comparison of these two graphs indicates reasonable behavior under grid refinement. Figure 8 shows a plot of the peak post-detonation pressure at each grid point for the 800 grid cell case. Note that the post-detonation pressure is approaching the Chapman–Jouguet pressure of 4,518,507 Pa.

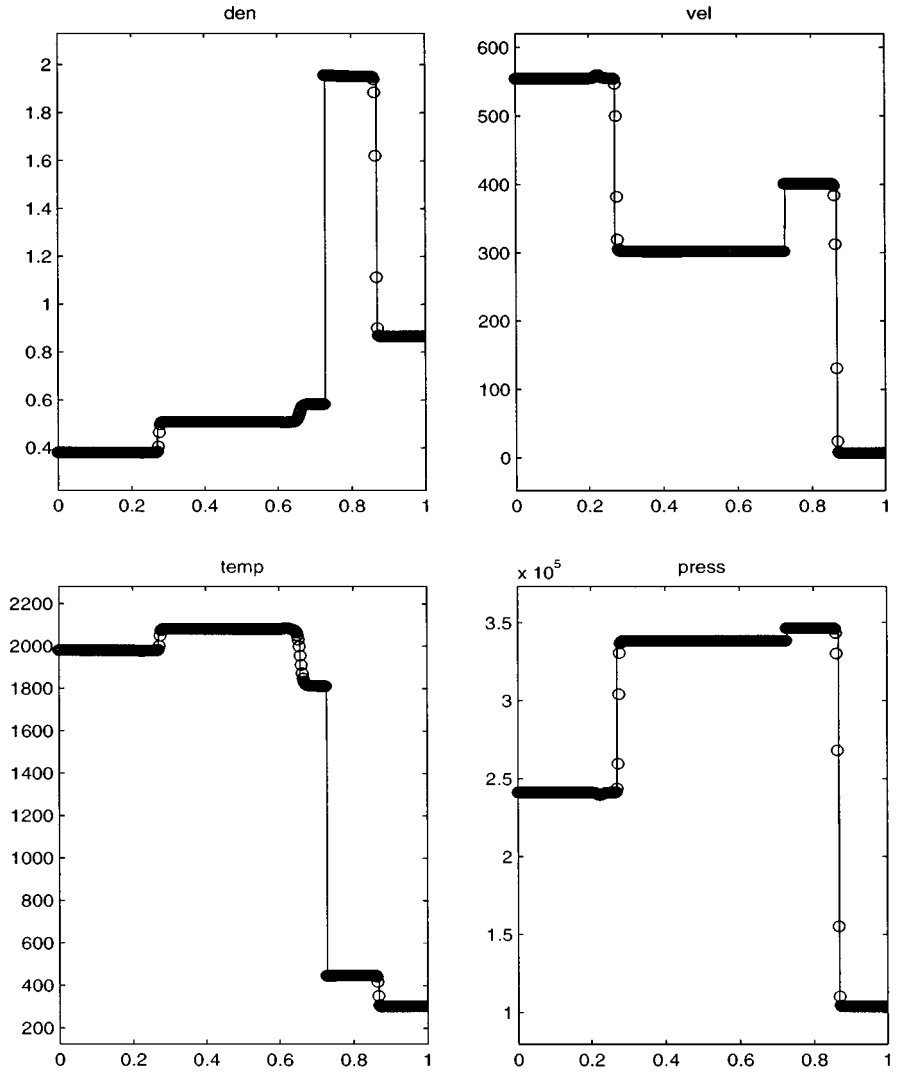

FIG. 11. Deflagration interaction with a rightgoing shock.

7.3. *Deflagrations*

For a deflagration, the unreacted material is represented by positive values of ϕ and the reacted material is represented by negative values of ϕ so that the unit normal points from the reacted material into the unreacted material. Equations (29), (30), and (31) are used along with Eq. (36), where the jump in e_o across the reaction front indicates the energy release in the chemical reaction. Equation (37) is still valid; however, since a deflagration is subsonic the "$\pm$" sign is chosen to give the minimum value of $|V_N^G - D|$ for both the reacted and the unreacted ghost fluids.

For a deflagration, the Riemann problem is not well posed unless the speed of the deflagration is given [13, 29]. Luckily, there is a large amount of literature on the G-equation for flame discontinuities. The G-equation was originally proposed in [17] and later discussed in [30]. The G-equation represents the flame front as a discontinuity in the same fashion

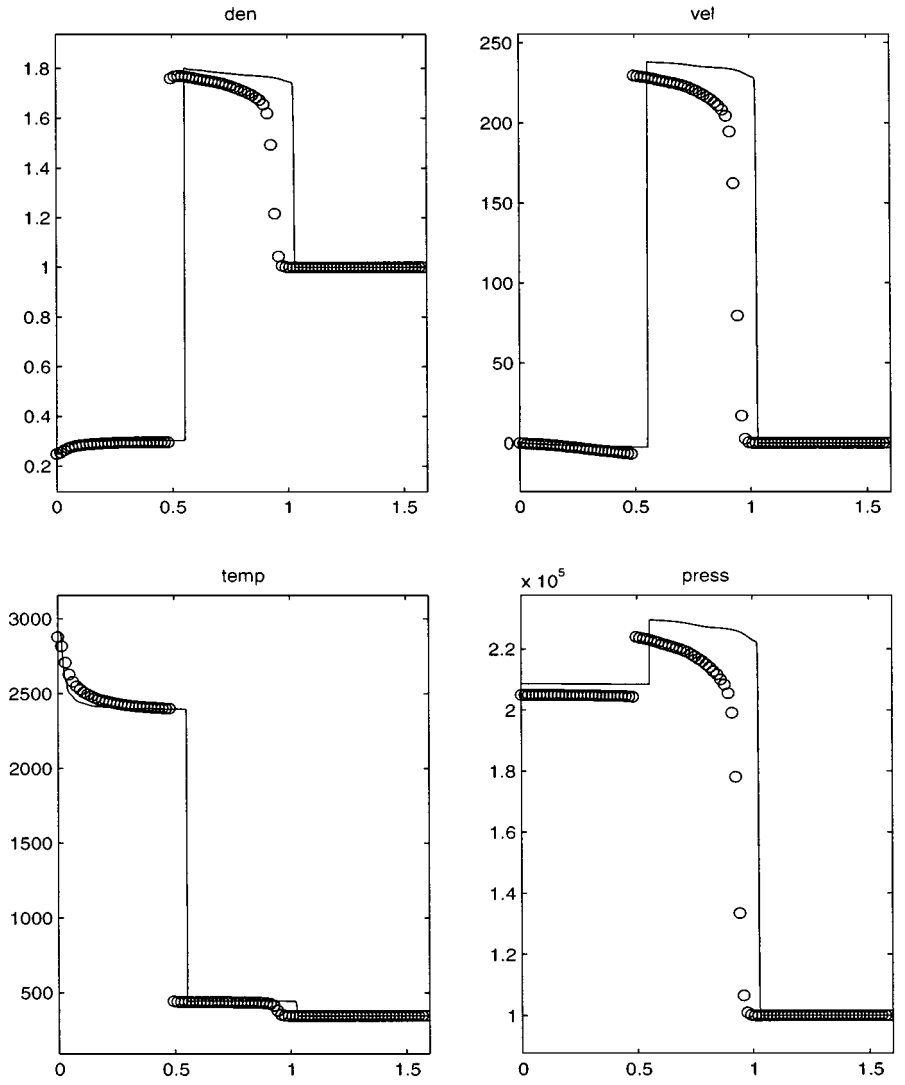

FIG. 12. Deflagration wave with a precursor shock wave—100 grid cells.

as the level set method. Thus, one can consult the literature on the G-equation to obtain deflagration speeds for the GFM.

7.3.1. EXAMPLE 5. In this example, we consider a single deflagration wave moving to the right with the deflagration velocity taken from [13, 29] as

$$D = V_N^{(2)} + \left(3.00 \times 10^{-9} \frac{\mathrm{s}^3}{\mathrm{m}^3}\right)\left(\frac{p^{(2)}}{\rho^{(2)}}\right)^2, \tag{38}$$

where we have redimensionalized the problem. Note that the superscript "(2)" stands for an unburnt gas quantity. We use a 1.6 m domain with 100 grid points and the interface located at $x = 0.8$ m which is exactly midway between the 50th and 51st grid points. We use $\gamma = 1.4$ and $M = 0.029$ kg/mol in both gases. Initially, we set $\rho = 0.142168$ kg/m^3, $u = -181.018$ m/s, and $p = 94{,}569.5$ Pa on the left, and $\rho = 1$ kg/m^3, $u = 0$ m/s, and $p = 1 \times 10^5$ Pa on the right. In addition, we have $e_o = 2.0 \times 10^6$ J/kg in the unburnt gas and

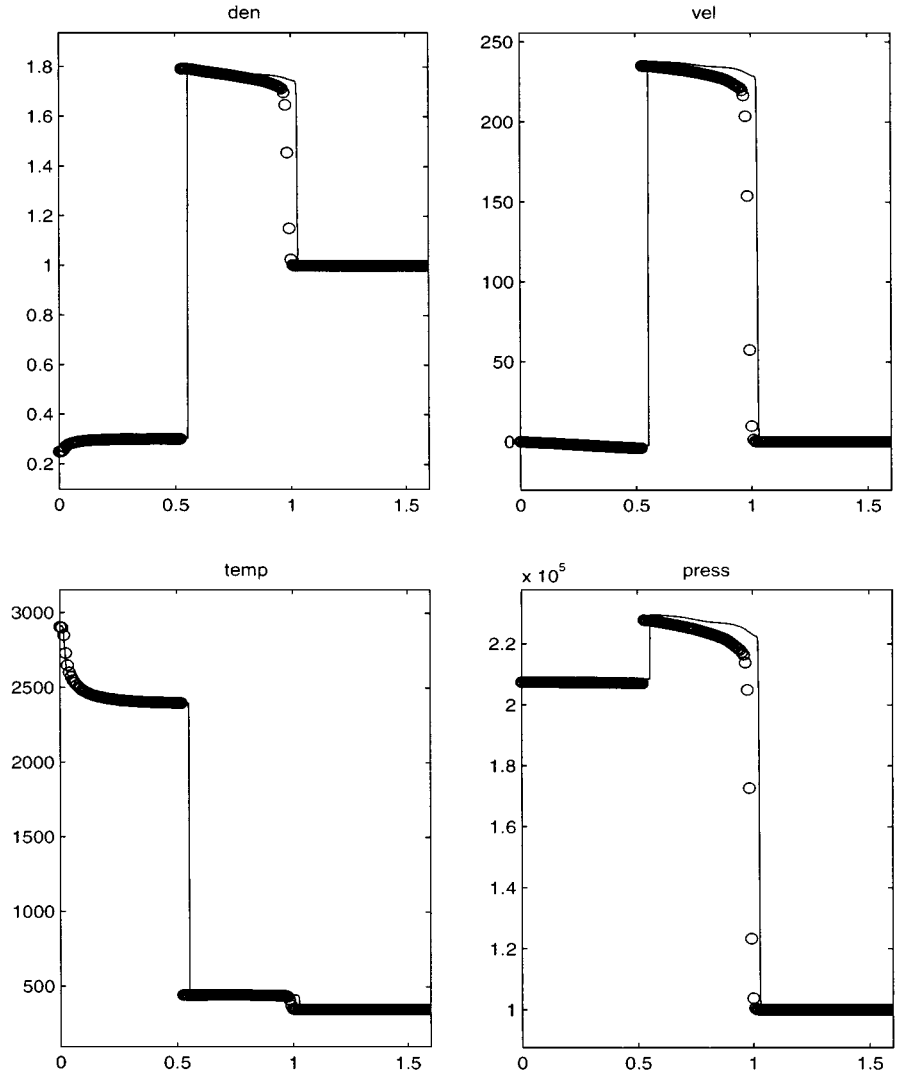

FIG. 13. Deflagration wave with a precursor shock wave—200 grid cells.

$e_o = 0$ in the burnt gas. Figure 9 shows the solution at $t = 0.01$ s after it has moved from $x = 0.8$ m to about $x = 1.1$ m at a speed of about 30.0 m/s. The exact solution is plotted as a solid line in the figure.

7.3.2. EXAMPLE 6. In this example, we compare our results for shock deflagration interactions with exact solutions from [20] using the deflagration velocity

$$D = V_N^{(2)} + 18.5\left(\frac{p^{(2)}}{101{,}000\ \text{Pa}}\right)^{.1}\left(\frac{T^{(2)}}{298\ \text{K}}\right)^{1.721}\frac{\text{m}}{\text{s}}, \tag{39}$$

where the superscript "(2)" stands for an unburnt gas quantity. We use a 1 m domain with 400 grid points and the interface located at $x = 0.5$ m. We use $\gamma = 1.4$, $M = .021$ kg/mol, and $e_o = 3.38 \times 10^6$ J/kg in the unburnt gas corresponding to a stoichiometric hydrogen air

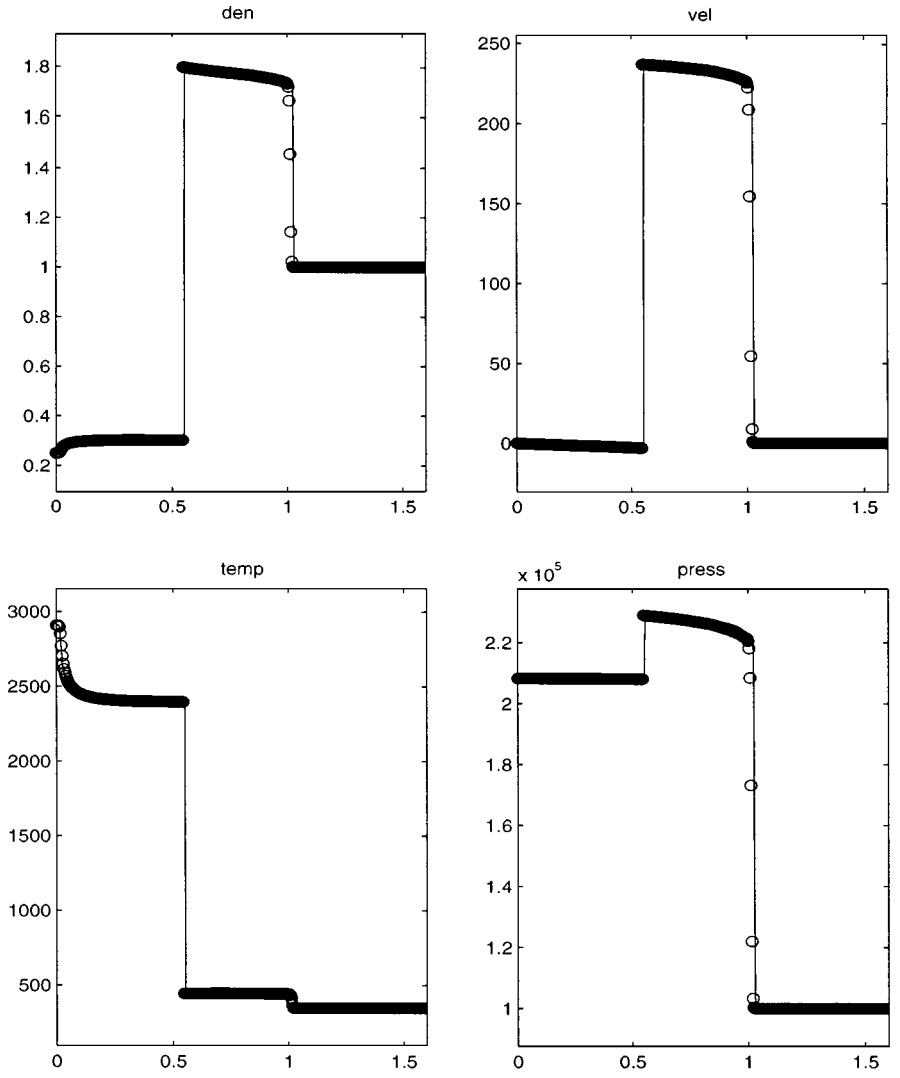

FIG. 14. Deflagration wave with a precursor shock wave—400 grid cells.

mixture. We use $\gamma = 1.17$, $M = 0.026$ kg/mol, and $e_o = 0$ in the burnt gas. The burnt gas is one the left of the interface and the unburnt gas is on the right of the interface.

The first case consists of a leftgoing shock starting at $x = 0.6$ m with preshock states of $\rho = 1.587$ kg/m^3, $u = 283.2$ m/s, and $p = 249{,}900$ Pa on the left, and postshock states of $\rho = 2.128$ kg/m^3, $u = 139.9$ m/s, and $p = 378{,}200$ Pa on the right. The burnt gas has initial states of $\rho = 0.4289$ kg/m^3, $u = 194.8$ m/s, and $p = 244{,}800$ Pa. The shock hits the deflagration and the collision results in four waves shown in Fig. 10 at $t = 0.00065$ s as a shock, contact, deflagration, and rarefaction from left to right. All waves are captured, except the deflagration wave which is tracked with the level set function. The results agree well with the exact solution, which is plotted as a solid line in the figure.

The second case consists of a rightgoing shock starting at $x = 0.4$ m with postshock states of $\rho = 0.3809$ kg/m^3, $u = 555.1$ m/s, and $p = 241{,}100$ Pa on the left, and preshock states of $\rho = 0.1859$ kg/m^3, $u = -61.96$ m/s, and $p = 102{,}700$ Pa on the right. The unburnt gas

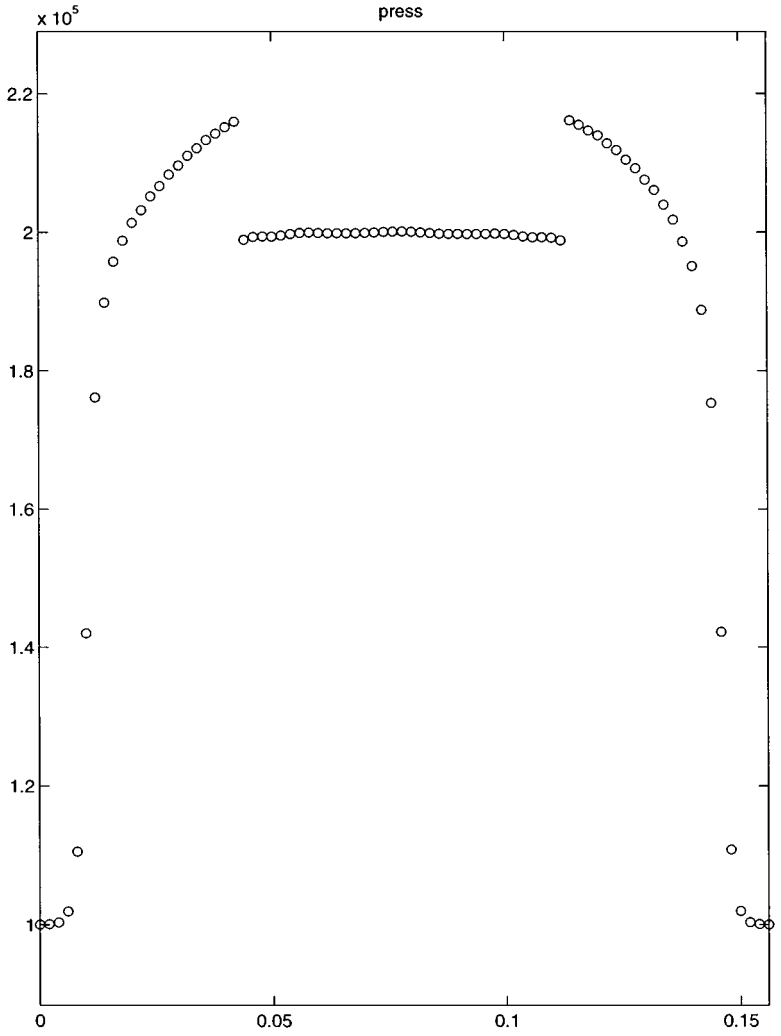

FIG. 15. Deflagration waves with precursor shock waves.

has initial states of $\rho = 0.8672$ kg/m^3, $u = 6.762$ m/s, and $p = 103{,}900$ Pa. The shock hits the deflagration and the collision results in four waves shown in Fig. 11 at $t = 0.0006$ s as a shock, contact, deflagration, and shock from left to right. All waves are captured, except the deflagration wave, which is tracked with the level set function. The results agree well with the exact solution, which is plotted as a solid line in the figure.

7.3.3. EXAMPLE 7. Next, we take the deflagration from Example 5 and enforce a solid wall boundary condition at $x = 0$. It is important to note that a reflection boundary condition is applied to the level set function as well. That is, we start with $\phi = x - 0.024$ m and after applying the reflection boundary condition we have $\phi = |x| - 0.024$ m as initial data. This initial data assumes that the entire domain is unburnt (the right state in Example 5), except for a small region near the solid wall which we assume to be burnt (the left state in Example 5).

Due to the influence of the solid wall, we initially set the velocity of the burnt state to be identically zero (not -181.018 m/s). Since the solid wall prevents the deflagration from accelerating the burnt gas to the left, a shock wave forms to the right of the deflagration.

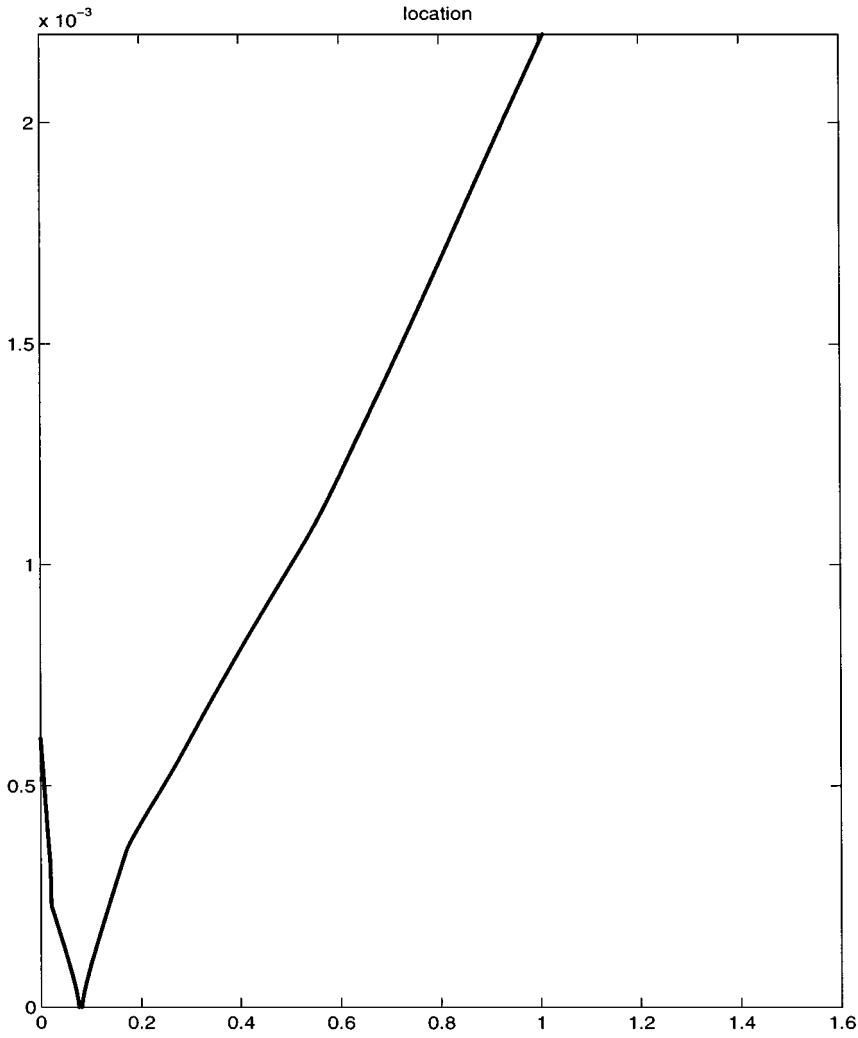

FIG. 16. Deflagration wave location (time vs space).

This shock wave pre-accelerates the unburnt gas to the right, so that the acceleration of the gas to the left by the deflagration wave is approximately canceled, resulting in a burnt gas velocity near zero as forced by the solid wall.

The circles in Fig. 12 show the deflagration wave computed with 100 grid cells (101 grid points) at $t = 0.002$ s when it is located near $x = 0.5$ m moving to the right at approximately 278 m/s. Note the captured shock wave near $x = 1$ m. In Figs. 13 and 14 the same calculation was carried out with 200 grid cells (201 grid points) and 400 grid cells (401 grid points), respectively. For the sake of comparison, a more refined calculation with 800 grid cells (801 grid points) is plotted as a solid line in all three figures. These figures illustrate first order convergence in the location of the discontinuous deflagration wave and the captured shock wave. In addition, note that the overheating errors in temperature and density at the wall could be minimized with the Isobaric Fix [8].

An important technical detail concerns the treatment of the normal in the burnt region near the wall. Consider the 101 grid point case where there are initially three burnt points

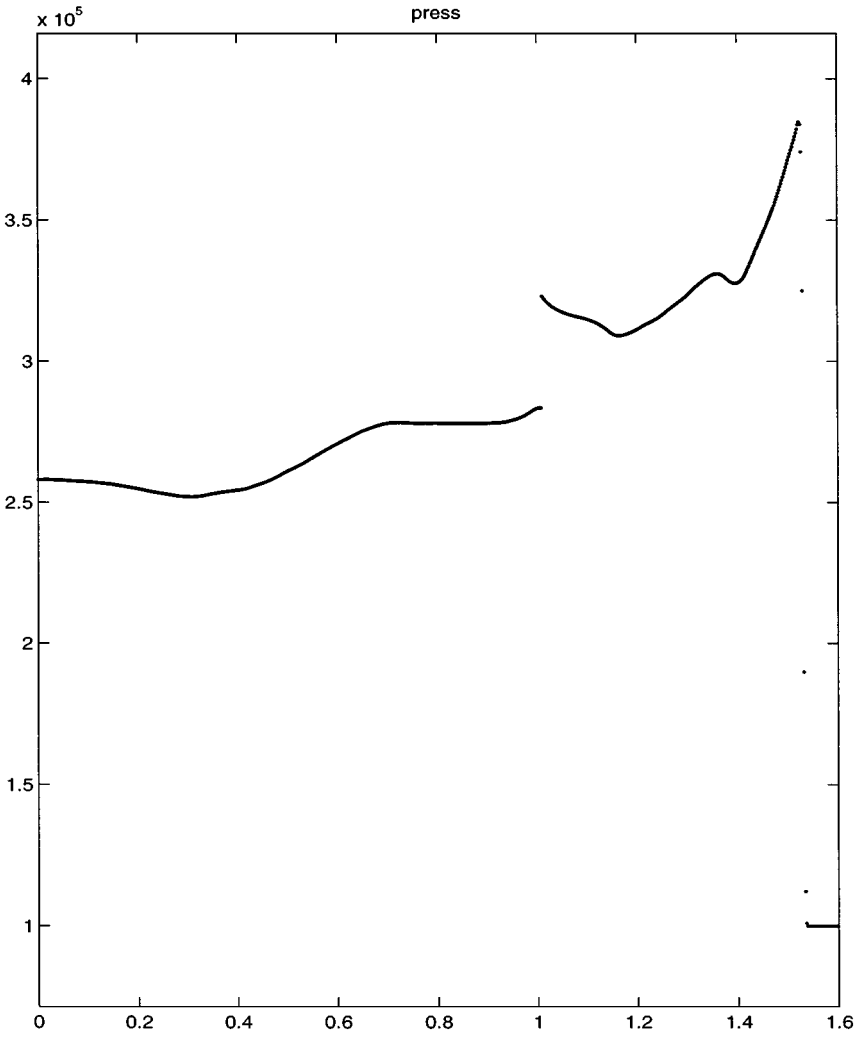

FIG. 17. Deflagration wave at $t = 0.0022$ s.

consisting of one at $x = 0$, one to the right of $x = 0$, and a solid wall boundary reflected point just to the left of $x = 0$. The normal **N** will be undefined at $x = 0$ if standard central differencing is used to compute it. Thus, one must be careful when computing **N** with a standard central difference. In these cases we resort to one-sided differencing to compute the normal. In this particular example, essentially equivalent results are obtained regardless of which direction we use to compute the one-sided difference. Inherently, this is a problem with level sets in under-resolved regions since local extrema may occur near the zero level. However, this is a problem only when the extrema are positioned exactly on a grid node, which is unusual except for initial data. For our purposes, we address this problem by assigning a normal in an arbitrary direction by choosing one-sided differencing in an arbitrary direction.

7.3.4. EXAMPLE 8. Once again, we consider deflagration waves with velocities determined by Eq. 38. We use a 1.6 m domain with 801 grid points and a solid wall boundary condition at $x = 0$. Initially, $\phi = |x - 0.078\ \text{m}| - 0.003\ \text{m}$, where the three grid points at

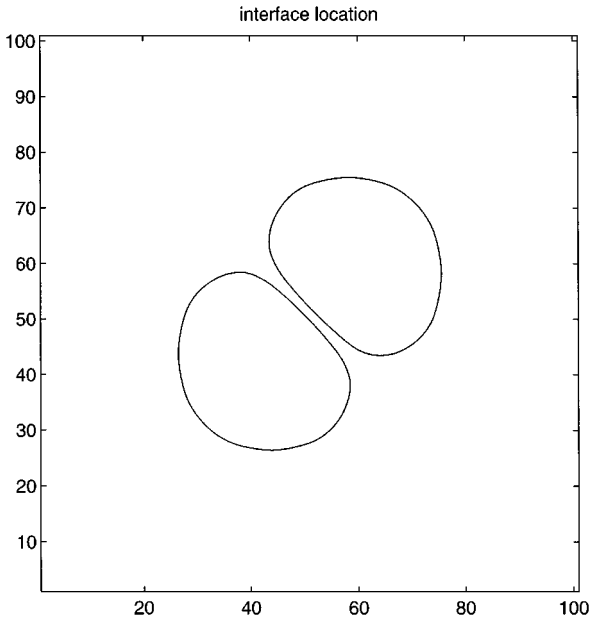

FIG. 18. Interface locations before merging—0.0008 s.

$x = 0.076$ m, $x = 0.078$ m, and $x = 0.08$ m designate a burnt gas with $\rho = 0.2082$ kg/m^3, $u = 0$ m/s, $p = 140{,}720$ Pa, and $e_o = 0$. The rest of the domain is an unburnt gas with $\rho = 1$ kg/m^3, $u = 0$ m/s, $p = 1 \times 10^5$ Pa, and $e_o = 2.0 \times 10^6$ J/kg. In both gases, $\gamma = 1.4$ and $M = 0.029$ kg/mol.

The solution consists of two deflagration waves moving outward from $x = 0.078$ m (in opposite directions). Since the burnt gas is confined between these deflagrations, it must

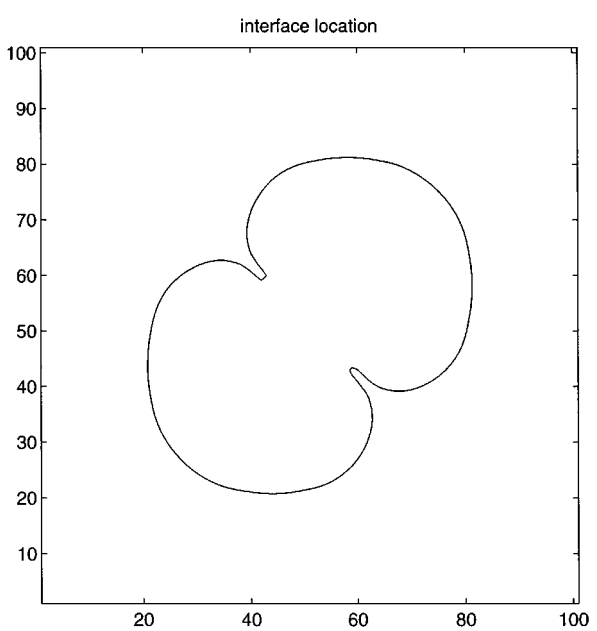

FIG. 19. Interface locations after merging—0.001 s.

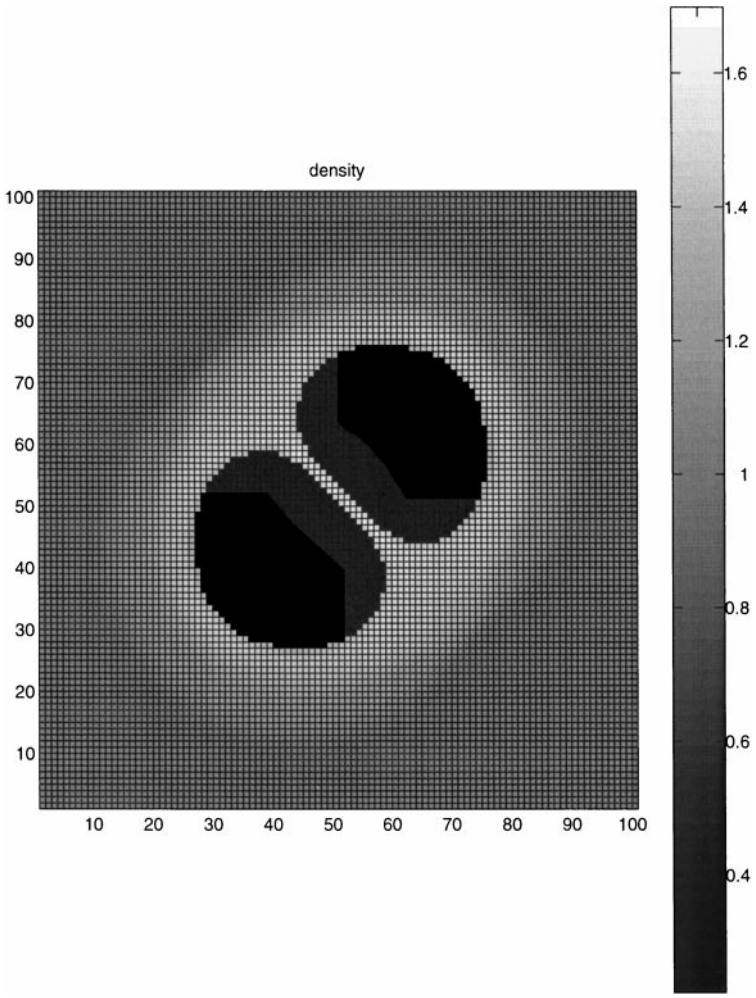

FIG. 20. Interface locations before merging—0.0008 s.

have a near zero velocity inducing shock waves in front of the deflagrations, as can be seen in Fig. 15 at $t = 0.000147$ s, where the deflagrations are located near $x = 0.043$ and $x = 0.113$ and the shocks are located near $x = 0.01$ and $x = 0.146$.

The leftgoing shock wave will reflect off the solid wall boundary, change direction, and then intersect the leftgoing deflagration near $x = 0.02$ m, causing it to slow down (although it eventually reaches the wall and burns out). The transmitted shock eventually catches up with the rightgoing deflagration near $x = 0.175$ m, causing it to accelerate to the right. The resulting transmitted shock will eventually overtake the lead rightgoing shock. Figure 16 shows a time history of the location of the deflagration waves and Fig. 17 shows the pressure at $t = 0.0022$ s.

7.4. *Multidimensions*

In multidimensions, the normal velocity is defined by $V_N = \mathbf{V} \cdot \mathbf{N}$, Eq. 14 is still

$$F_\rho = \rho(V_N - D) \tag{40}$$

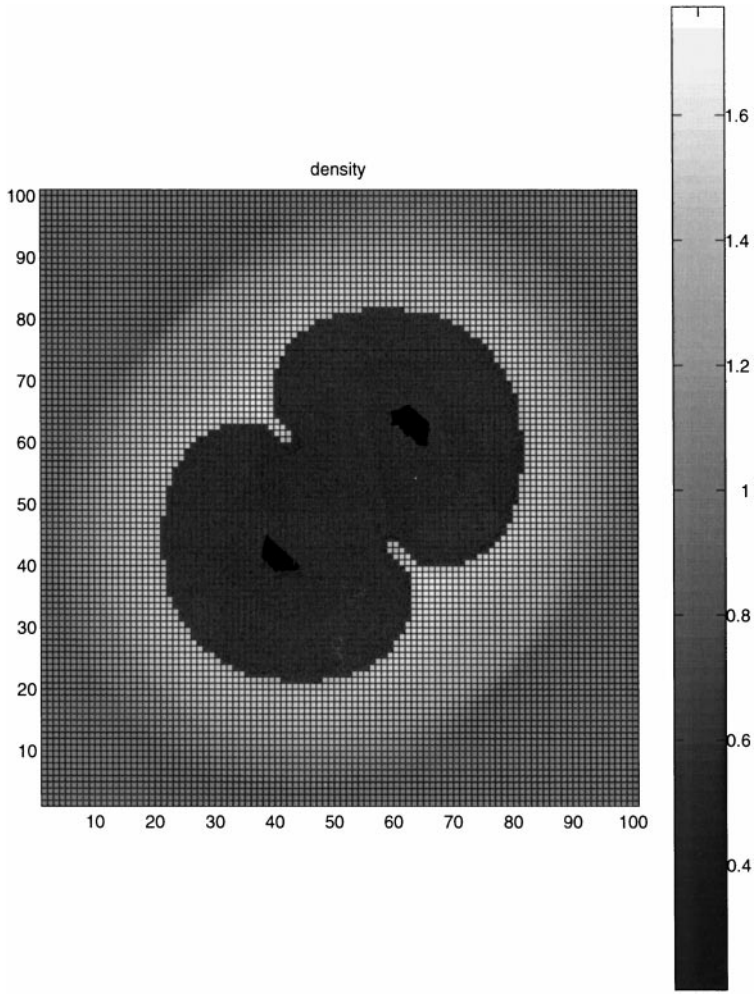

FIG. 21. Interface locations after merging—0.001 s.

and Eq. 27 is still

$$F_{\rho \mathbf{v}_N} = \mathbf{N}\mathbf{F}_{\rho \mathbf{v}} = \rho(V_N - D)^2 + p \tag{41}$$

while

$$\mathbf{F}_{\rho \mathbf{v}_T} = \frac{\mathbf{F}_{\rho \mathbf{v}} - F_{\rho \mathbf{v}_N}\mathbf{N}^T}{F_\rho} = \mathbf{V}^T - V_N \mathbf{N}^T \tag{42}$$

is valid when $V_N \neq D$, i.e., except for the case of a contact discontinuity. The necessary continuity of this expression implies the well known fact that tangential velocities are continuous across shocks, detonations, and deflagrations. Note that tangential velocities are not necessarily continuous across contact discontinuities.

Note that

$$|\mathbf{V} - D\mathbf{N}|^2 = |\mathbf{V}|^2 - 2DV_N + D^2 = |\mathbf{V}|^2 - V_N^2 + (V_N - D)^2 \tag{43}$$

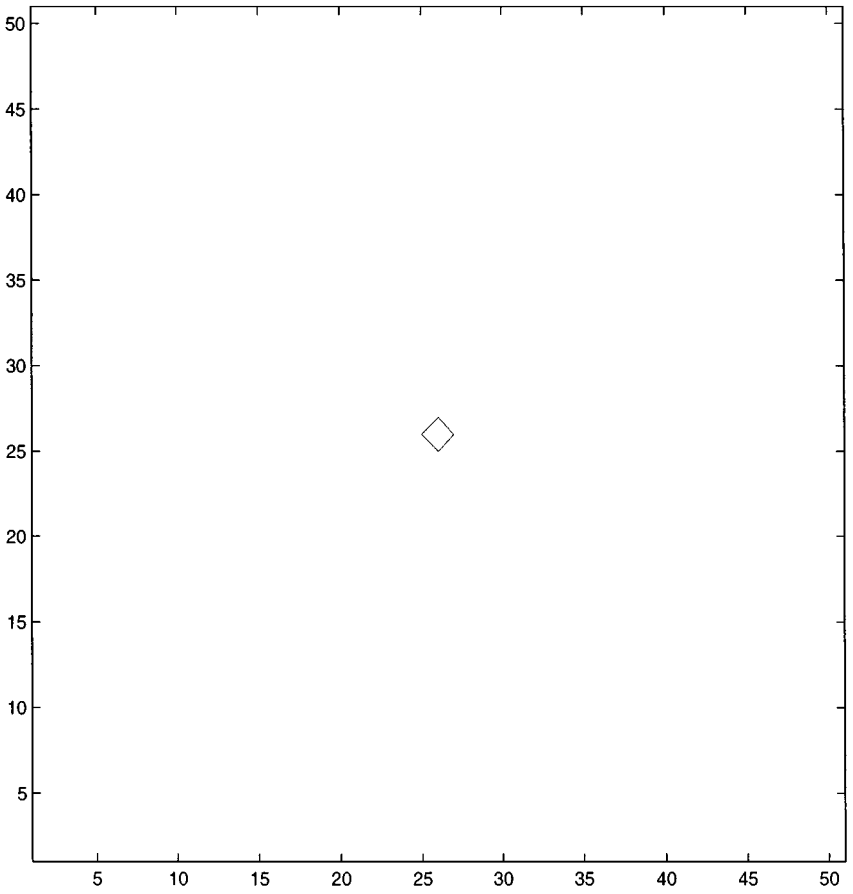

FIG. 22. Initial data—50 grid cells in each direction.

and

$$|\mathbf{V}|^2 = V_N^2 + V_{T_1}^2 + V_{T_2}^2, \tag{44}$$

where V_{T_1} and V_{T_2} are the velocities in the tangent directions T_1 and T_2, respectively. Combining Eqs. (43) and (44) yields

$$|\mathbf{V} - D\mathbf{N}|^2 = V_{T_1}^2 + V_{T_2}^2 + (V_N - D)^2, \tag{45}$$

which can plugged into Eq. 16 to obtain

$$F_E = \left(\rho e + \frac{\rho\left(V_{T_1}^2 + V_{T_2}^2\right)}{2} + \frac{\rho(V_N - D)^2}{2} + p\right)(V_N - D) \tag{46}$$

as a rewritten version of Eq. (16).

Defining

$$\hat{F}_E = F_E - \frac{F_\rho\left(V_{T_1}^2 + V_{T_2}^2\right)}{2} = \left(\rho e + \frac{\rho(V_N - D)^2}{2} + p\right)(V_N - D) \tag{47}$$

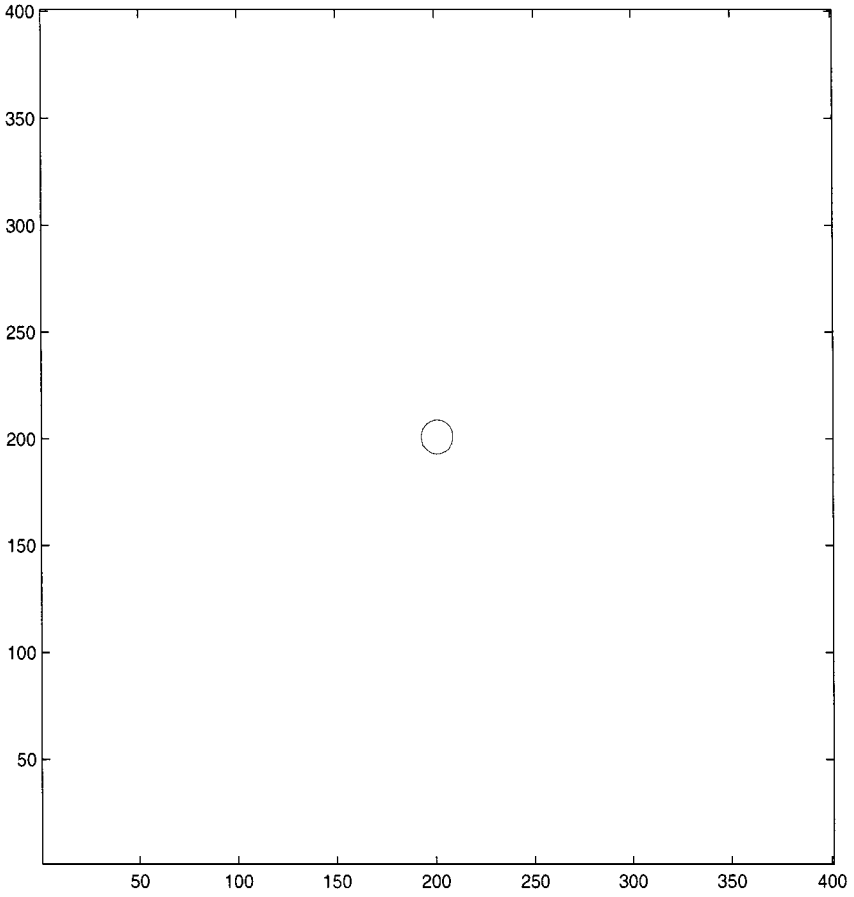

FIG. 23. Initial data—400 grid cells in each direction.

and using this equation along with Eqs. (40) and (41) and the equation of state for the ghost fluid

$$p^G = (\gamma^G - 1)\rho^G\left(e^G - e_o^G\right) \tag{48}$$

lead to

$$V_N^G - D = \frac{\gamma^G F_{\rho \mathbf{V}_N}^R}{(\gamma^G + 1)F_\rho^R} \pm \sqrt{\left(\frac{\gamma^G F_{\rho \mathbf{V}_N}^R}{(\gamma^G + 1)F_\rho^R}\right)^2 - \frac{2(\gamma^G - 1)}{(\gamma^G + 1)}\left(\frac{\hat{F}_E^R}{F_\rho^R} - e_o^G\right)}, \tag{49}$$

which is identical to Eq. (37) in every way, since the definition of $\hat{F}_E$ in multidimensions is identical to the definition of F_E in one dimension.

To summarize, Eq. (49) can be used to find V_N^G, with the proper choice of the "$\pm$" sign outlined in the one dimensional cases. Then Eq. (40) can be used to find ρ^G, Eq. (41) can be used to define p^G, and Eq. (48) can be used to find e^G. The velocity, $\mathbf{V}^G$, is obtained by combining the normal velocity of the ghost fluid with the tangential velocity of the real fluid through the equation

$$\mathbf{V}^G = \mathbf{V}_N^G\mathbf{N} + \mathbf{V}^R - V_N^R\mathbf{N}, \tag{50}$$

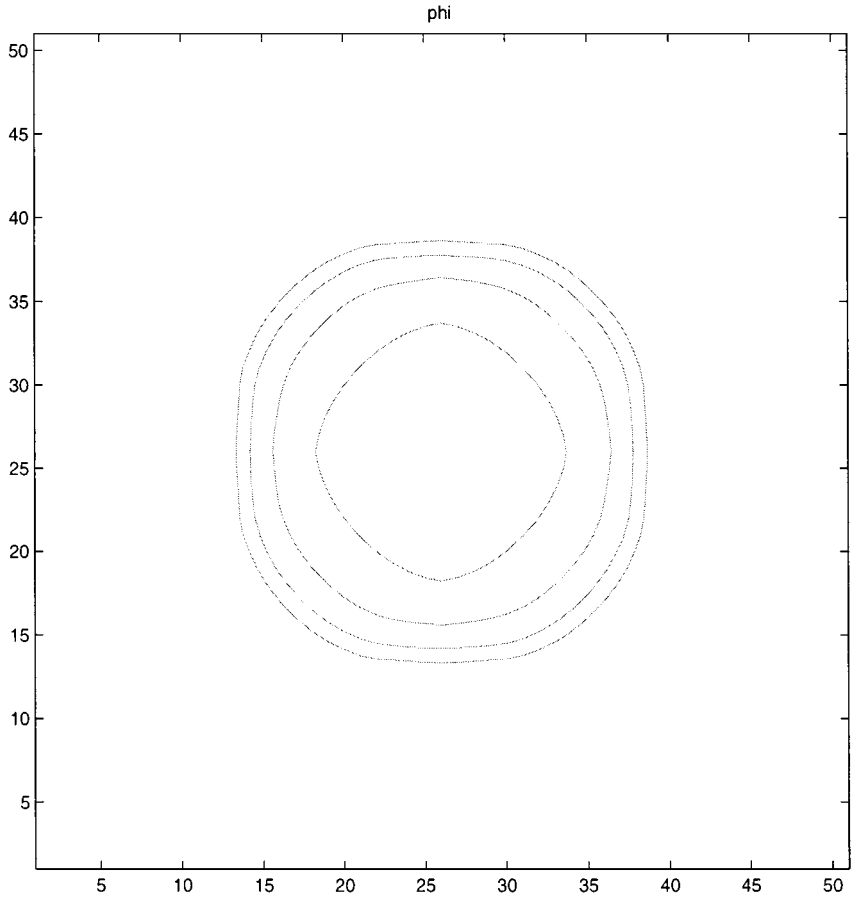

FIG. 24. 50, 100, 200, and 400 grid cells in each direction.

where $V_N^R = \mathbf{V}^R \cdot \mathbf{N}$ is the normal velocity of the real fluid. Note that the tangent directions are never explicitly used, so that the method is simple to implement in three spatial dimensions.

7.4.1. EXAMPLE 9. This example is similar to the example in Section 5.1 of [27]. Consider a 1 m square domain with 100 grid cells in each direction. Two circular regions of burnt gas are centered at (0.425 m, 0.425 m) and at (0.575 m, 0.575 m) with a radius of 0.02 m each. The rest of the domain is defined as unburnt gas. Both the burnt gas and the unburnt gas are defined as in Example 5, except that we set $u = v = 0$ m/s in the burnt gas as in Example 7.

In each circular region, a shock wave will form and travel outward, preaccelerating the unburnt gas similarly to the one-dimensional result calculated in Example 7. Since there are two circular regions, these shock waves will intersect each other and interfere with the circular growth of the burnt regions distorting their shape. Figures 18 and 19 show the interface locations before and after merging, corresponding to 0.0008 and 0.001 s, respectively.

In Figs. 20 and 21 we plot square cells which are color coded based on the density values at the cell centers. A color bar is included to the right of each figure to illustrate the discontinuous density profile at the interface. The density jumps more than 1 kg/m^3 without

the presence of spurious intermediate values due to numerical dissipation. Note that the "white" region away from the interface is due to shock wave compressions.

7.4.2. EXAMPLE 10. Consider one of the 0.02 m radius circular regions of burnt gas from Example 9 located in the center of the computational domain at (0.5 m, 0.5 m). In order to illustrate the effects of grid refinement, calculations are carried out with 50, 100, 200, and 400 grid cells in each direction. Note that the case with 50 grid cells in each direction is rather coarse and that large errors are already present in the initial data due to grid representation errors as shown in Fig. 22. Compare this with Fig. 23, which shows the initial data for the case with 400 grid cells in each direction. Figure 24 shows the interface locations for each case at a final time of 0.001 s. The calculations demonstrate first order convergence for the location of the interface, although grid effects are apparent due in part to the poor resolution of the initial data.

REFERENCES

1. D. Adalsteinsson and J. A. Sethian, The fast construction of extension velocities in level set methods, *J. Comput. Phys*. **148**, 2 (1999).
2. T. Aslam, A level set algorithm for tracking discontinuities in hyperbolic conservation laws. II. Systems of equations, in preparation.
3. P. Atkins, *Physical Chemistry* (Freeman, New York, 1994), 5th ed.
4. I.-L. Chern and P. Colella, *A Conservative Front Tracking Method for Hyperbolic Conservation Laws*, UCRL-97200, LLNL, July 1987.
5. J.-P. Cocchi and S. Saurel, A Riemann problem based method for the resolution of compressible multimaterial flows, *J. Comput. Phys.* **137**, 265 (1997).
6. S. Davis, An interface tracking method for hyperbolic systems of conservation laws, *Appl. Numer. Math*. **10**, 447 (1992).
7. R. Fedkiw, T. Aslam, B. Merriman, and S. Osher, A non-oscillatory Eulerian approach to interfaces in multimaterial flows (the Ghost Fluid Method), *J. Comput. Phys*. **152**, 457 (1999).
8. R. Fedkiw, A. Marquina, and B. Merriman, An isobaric fix for the overheating problem in multimaterial compressible flows, *J. Comput. Phys.* **148**, 545 (1999).
9. R. Fedkiw, B. Merriman, and S. Osher, Efficient characteristic projection in upwind difference schemes for hyperbolic systems (the Complementary Projection Method), *J. Comput. Phys.* **141**, 22 (1998).
10. R. Fedkiw, B. Merriman, and S. Osher, High accuracy numerical methods for thermally perfect gas flows with chemistry, *J. Comput. Phys.* **132**, 175 (1997).
11. R. Fedkiw, B. Merriman, and S. Osher, Simplified discretization of systems of hyperbolic conservation laws containing advection equations, submitted for publication.
12. R. Fedkiw, B. Merriman, and S. Osher, Numerical methods for a one-dimensional interface separating compressible and incompressible flows, in *Barriers and Challenges in Computational Fluid Dynamics*, edited by V. Venkatakrishnan, M. Salas, and S. Chakravarthy (Kluwer Academic, Norwell, MA, 1998), pp. 155–194.
13. J. Hilditch and P. Colella, A front tracking method for compressible flames in one dimension, *SIAM J. Sci. Comput*. **16**, No. 4, 755 (July 1995).
14. S. Karni, Multicomponent flow calculations by a consistent primitive algorithm, *J. Comput. Phys*. **112**, 31 (1994).
15. R. Klein, Personal communication.
16. X-D. Lius and S. Osher, Convex ENO high order schemes without field-by-field decomposition or staggered grids, *J. Comput. Phys.* **142**, 304 (1998).
17. G. H. Markstein, *Nonsteady Flame Propagation* (Pergamon, Oxford, 1964).
18. V. Moser, F. Zhang, and P. Thibault, Detonation front tracking via incell reconstruction, in *Proceedings, 3rd Annual, Conference of the CFD society of Canada, Banff, 1995*.

19. W. Mulder, S. Osher, and J. A. Sethian, Computing interface motion in compressible gas dynamics, *J. Comput. Phys*. **100**, 209 (1992).
20. S. R. Mulpuru and G. B. Wilkin, Finite difference calculations of unsteady premixed flame–flow interactions, *AIAA J.* **23**, No. 1 (January 1985).
21. S. Osher and J. A. Sethian, Fronts propagating with curvature dependent speed: Algorithms based on Hamilton–Jacobi formulations, *J. Comput. Phys.* **79**, No. 1, 12 (1988).
22. R. Pember, J. Bell, P. Colella, W. Crutchfield, and M. Welcome, An adaptive Cartesian grid method for unsteady compressible flow in irregular regions, *J. Comput. Phys.* **120**, 278 (1995).
23. J. A. Sethian, Curvature and the evolution of fronts, *Commun. Math. Phys.* **101**, 487 (1985).
24. C. W. Shu and S. Osher, Efficient implementation of essentially non-oscillatory shock capturing schemes, II, *J. Comput. Phys.* **83**, 32 (1989).
25. V. Smijanovski and R. Klein, Flame front tracking via in-cell reconstruction, in *Proceedings, 5th International Conference on Hyperbolic Problems, Theory, Numerics, and Applications, 1995*.
26. V. Smiljanovski and R. Klein, Simulation of gas dynamic flame instability and DDT using in-cell reconstruction, in *Proceedings, 6th International Symposium on CFD, Lake Tahoe, NV, 1995*.
27. V. Smiljanovski, V. Moser, and R. Klein, A capturing–tracking hybrid scheme for deflagration discontinuities, *Combust. Theory Modeling* **1**, 183 (1997).
28. M. Sussman, P. Smereka, and S. Osher, A level set approach for computing solutions to incompressible two-phase flow, *J. Comput. Phys.* **114**, 146 (1994).
29. Z.-H. Teng, A. Chorin, and T.-P. Liu, Riemann problems for reacting gas with applications to transition, *SIAM J. Appl. Math.* **42**, No. 5 (October 1982).
30. F. A. Williams, in *The Mathematics of Combustion*, edited by J. D. Buckmaster (SIAM, Philadelphia, 1985), pp. 97–131.